

## Article

# The Hidden Magmatic Chamber from the Ponte Nova Mafic–Ultramafic Alkaline Massif, SE Brazil: Clues from Clinopyroxene and Olivine Antecrysts

Rogério Guitarrari Azzone <sup>1,\*</sup>, Lina Maria Cetina Tarazona <sup>1,2</sup>, Mariana Robertti Ambrosio <sup>1,2</sup>,  
Vincenza Guarino <sup>3,\*</sup>, Luanna Chmyz <sup>1</sup>, Nicholas Machado Lima <sup>4</sup> and Excelso Ruberti <sup>1</sup>

<sup>1</sup> Department of Mineralogy and Geotectonics, Institute of Geosciences (IGc), University of São Paulo (USP), São Paulo 05508-080, Brazil; linacetina0526@usp.br (L.M.C.T.); mariana.robertti.ambrosio@usp.br (M.R.A.); chmyz@usp.br (L.C.); exrubert@usp.br (E.R.)

<sup>2</sup> Postgraduate Program for Geosciences (Mineralogy and Petrology), Institute of Geosciences (IGc), University of São Paulo (USP), São Paulo 05508-080, Brazil

<sup>3</sup> Dipartimento di Scienze della Terra, dell'Ambiente e delle Risorse, Università di Napoli Federico II, 80138 Naples, Italy

<sup>4</sup> Petróleo Brasileiro S.A., Centro de Pesquisa e Desenvolvimento Leopoldo Miguez de Mello (CENPES), Rio de Janeiro 21941-915, Brazil; nicholasgeo91@gmail.com

\* Correspondence: rgazzone@usp.br (R.G.A.); vincenza.guarino@unina.it (V.G.)

**Abstract:** Clinopyroxene and olivine primocrysts in the intrusions of the Ponte Nova mafic–ultramafic alkaline massif (SE Brazil) present several textures and zoning that indicate open-system processes. Important compositional differences were found in the clinopyroxene. Diopside relict cores (mostly partially corroded) present higher Mg, Cr and Ni and lower Ti, Na, Al, REE and Sr than Ti-augite mantling and rims. Subordinately, two types of olivine crystals were recognized, one related to very zoned crystals with high Mg (Fo up to 86 mol.%) and Ni cores (mostly with corroded rims), and other almost without clear zonation and with lower Mg contents. Relict cores of high-Mg clinopyroxene and olivine crystals are representative of antecrysts formed in deeper chamber environments. Temperature and pressure estimates based on clinopyroxene–liquid geothermobarometers indicate crystallization of the antecrysts at  $\sim 1171 \pm 10$  °C and  $\sim 5.7 \pm 0.3$  kbar, pointing to a deeper hidden magmatic chamber, whereas mantling and rim compositions indicate a shallow chamber environment. Clinopyroxenes of this hidden chamber have progressive enrichments of incompatible elements with the Mg# decrement and inflection points in Sr and REE due to the starting of co-precipitation of apatite. The evolution trend of clinopyroxene antecrysts indicates that the main intrusions in the Ponte Nova shallow chamber were fed by a single deeper hidden chamber mainly controlled by typical fractional crystallization processes. These antecrysts indicate the presence of a complex plumbing system, which is also supported by similar antecrysts found in the lamprophyre and alkali basalt dikes of this region. The preferred petrological model for the Ponte Nova massif could be summarized as repeated influxes of antecryst-laden basanite magmas that deposited most of their suspended crystals on the floor of the upper-crust magma chamber.

**Keywords:** antecrysts; complex plumbing system; olivine; clinopyroxene; alkaline magmatism; REE; Ponte Nova massif; Brazil



**Citation:** Azzone, R.G.; Cetina, L.M.T.; Ambrosio, M.R.; Guarino, V.; Chmyz, L.; Lima, N.M.; Ruberti, E. The Hidden Magmatic Chamber from the Ponte Nova Mafic–Ultramafic Alkaline Massif, SE Brazil: Clues from Clinopyroxene and Olivine Antecrysts. *Minerals* **2022**, *12*, 775. <https://doi.org/10.3390/min12060775>

Academic Editor: Andrei Y. Barkov

Received: 17 May 2022

Accepted: 16 June 2022

Published: 18 June 2022

**Publisher's Note:** MDPI stays neutral with regard to jurisdictional claims in published maps and institutional affiliations.



**Copyright:** © 2022 by the authors. Licensee MDPI, Basel, Switzerland. This article is an open access article distributed under the terms and conditions of the Creative Commons Attribution (CC BY) license (<https://creativecommons.org/licenses/by/4.0/>).

## 1. Introduction

Magmas generated at different pressures in the mantle will ascend through the lithosphere, possibly lodge in intermediate reservoirs, and ultimately find their final emplacement sites along a network of interconnected channels, like a plumbing system [1–8]. Such a complex system allows for cogenetic and/or captured crystals (antecrysts or xenocrysts, respectively) to be recycled during the ascent of magmas through the lithosphere. As minerals record changes in the magmatic environment, the information of each chamber

may be preserved in their zoning patterns (growth stratigraphy, [9]) and thus be revealed by petrography and in situ analyses of each of the different zones. This mechanism allows the identification of early magmatic stages and associated processes [3,9–11].

In a complex plumbing system of mantle-derived silica-undersaturated magmas (alkaline magmas), various types of processes and mechanisms of magmatic evolution are involved, including those representatives of open systems. These processes can be well recognized in the study of plutonic and hypabyssal intrusions, with evidence of evolution in open systems being found: (i) at the mega- and macroscale, from geological features observed in the field (e.g., schlieren banding, enclaves, crustal xenoliths with evidence of partial melting or dissolution/digestion, hybridization structures, etc.), complemented by whole-rock analysis of elemental and isotopic geochemistry (e.g., [12–17]); (ii) at the microscale, from disequilibrium textures and complex zoning patterns of crystallized minerals, correlated with their main compositional tendencies (e.g., [9,18–20]); and (iii) at the submicroscopic scale, by cryptic variations in minerals recorded from trace element concentrations and isotopic signatures obtained through in-situ microanalysis (e.g., [4,5,10,21]).

Several hypabyssal occurrences are representative of complex plumbing systems, registering a combination of open-system processes in a trans-crustal system. Among the aforementioned records, although more commonly recognized in dikes and sills (e.g., [22–30]), antecrysts are also found in chamber environments (e.g., [31–34]). The slower cooling and extensive differentiation of plutons most usually hamper the unequivocal recognition of antecrysts, which tend to reequilibrate to the settling conditions ([10]) or even to completely dissolve (when as small crystals, [33]). However, recent studies show that even cumulate grains from large, layered intrusions (i.e., Bushveld Complex) are in fact antecrysts, injected from deeper magma chambers and then settled in a shallow chamber [35,36]. The latter would then present a hybrid composition resulting from the mixing of the new antecryst-laden magma batch and the resident magma [35].

A complex plumbing system model is assigned to the evolution of porphyritic basic–ultrabasic alkaline dikes from the Mantiqueira Range (southern Brazil), with porphyritic alkali basalts and lamprophyres holding macrocrysts representative of xenocrysts and antecrysts and unravelling magma mixing processes [37]. These dikes are from the Upper Cretaceous [38] and present similar ages and context with the Ponte Nova mafic–ultramafic alkaline massif (PN; [39]). The Upper Cretaceous basic–ultrabasic alkaline magmatism in the Mantiqueira region is part of the extensive Meso–Cenozoic continental alkaline–carbonatite magmatism that occurred in central and southeastern regions of the South American Platform [40]. The plumbing system evolution proposed for the Mantiqueira Range alkaline dikes indicate several stages of chamber-like environment, placed at different crustal levels [37]. The PN massif is an alkaline body representative of a shallow-level chamber environment [41]. It is composed of several intrusions, the main ones presenting cumulate character, being all olivine- and nepheline-normative rocks related to basanite parental magmas. The main arguments addressed in this work are the petrographic aspects and geochemical significance of olivine and clinopyroxene antecrysts identified in each intrusion of PN alkaline massif, where their geochemical changes strongly evidence the presence of a complex plumbing system related to the PN evolution.

## 2. Geological Setting

The Cretaceous alkaline occurrences from Southern Brazil are predominantly intrusive suites (<100 km<sup>2</sup>) composed of evolved lithotypes, mainly SiO<sub>2</sub>-saturated to SiO<sub>2</sub>-undersaturated syenites [42–45]. Mafic rocks are usually restricted to small intrusions (dikes, veins, stocks, plugs and pipes) or occur as cumulates associated with carbonatites complexes (Jacupiranga and Juquiá complexes). Among the alkaline intrusions cropping out along the coastal region of southern Brazil (Serra do Mar alkaline province, Figure 1A,B), only one plutonic suite shows prevalence of mafic–ultramafic rocks: the PN massif [39,41,46].

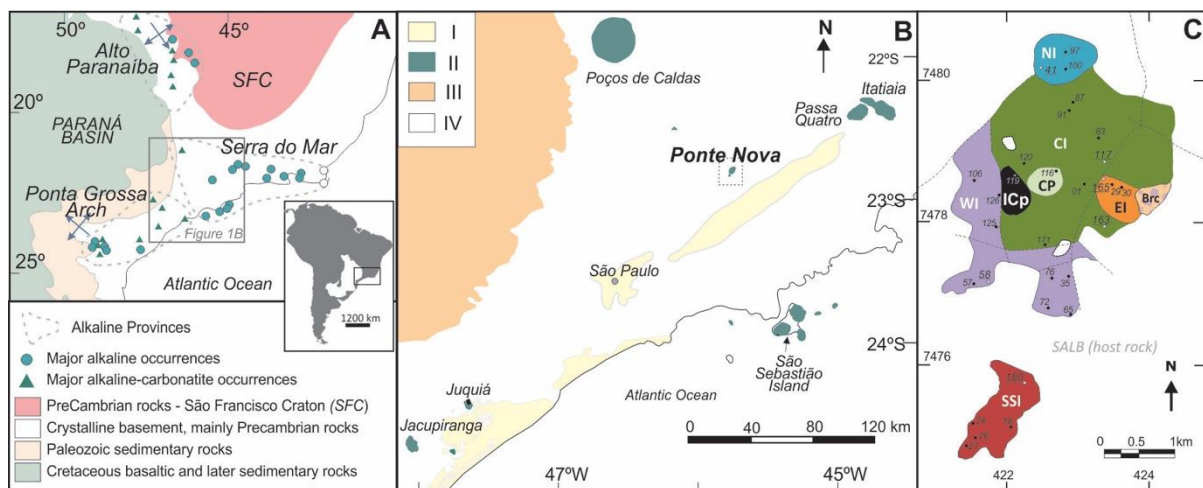


**Figure 1.** (A) Geological setting of the alkaline intrusions of Cretaceous magmatism in the southeastern part of Brazilian Platform, with the distribution of major alkaline occurrences of Alto Paranaíba, Serra do Mar and Ponta Grossa Arch alkaline provinces (Modified after [45]). (B) Detail of A, with the location of the main occurrences. Legend: I. Sediments or sedimentary rocks associated with rift basins (Cenozoic); II: Alkaline complexes (Meso-Cenozoic); III: Sedimentary rocks of the Paraná Basin (Ordovician-Silurian); IV: Crystalline Basement, Brasília and Ribeira orogenic belts (Precambrian). Simplified from [45]. (C) Simplified geological map of the Ponte Nova alkaline mafic-ultramafic massif [41]. Utilized abbreviations: CI, central intrusion; WI, western intrusion; NI, northern intrusion; EI, eastern intrusion; CP, central plug; SSI, southern satellite intrusion; ICp, ilmenite clinopyroxenites and magnetites; Brc, magmatic breccia; SALB: Serra de Água Limpa Batholith. Locations of studied samples are indicated as dots on the map; numbers in italic refer to samples analyzed by electron microprobe—wavelength dispersion system (EMP-WDS) and numbers in italic and underlined were analyzed by EMP-WDS and laser ablation—inductive coupled plasma mass spectrometry (LA ICP-MS).

The PN mafic-ultramafic alkaline massif (87.6 Ma; [39]) is an alkaline gabbroic association representative of several magmatic pulses (Figure 1C). Emplaced into Precambrian metagranites and gneiss of the Serra da Água Limpa Batholith (645–630 Ma, [47]), the PN consists of a main body (~5.5 km<sup>2</sup>) that encompasses five different intrusions (northern, central, western, and eastern intrusions and a central plug) and a smaller satellite body (southern satellite body; ~1 km<sup>2</sup>). For detailed geological and petrographic characteristics of the massif, the reader is referred to [39,41,48].

Most of the PN main body is represented by the central (CI) and western (WI) intrusions. The lower levels of CI and WI are composed of cumulatic melagabbros and clinopyroxenites (both with variable amounts of olivine), while their higher levels group monzogabbros with variable textural features (i.e., porphyritic, equigranular, massive, and banded rocks). The northern intrusion (NI) is also cumulatic, with olivine melamonzogabbros grading to olivine-bearing melamonzogabbros towards the top. The eastern intrusion (EI) is made up of more evolved types, monzodiorites with variable nepheline (inequigranular seriate and porphyritic textures). A small plug (CP) formed by porphyritic to equigranular microgabbros occupies the central part of the main body. The southern satellite intrusion (SSI) contains porphyritic nepheline-bearing melamonzonites and monzogabbros as predominant rocks, although more evolved types (i.e., nepheline-bearing monzonites) are also present. Other small intrusions cropping out in the interior of the massif include cumulates of sulfide-bearing ilmenite clinopyroxenites and magnetites (ICp), and a magmatic breccia (Brc). Numerous thin dikes of alkaline rocks of different degrees of evolution crosscut most PN intrusions, as well as the regional metagranitoids, being those widespread in the western Mantiqueira Range [38]. Especially, nearby the PN

massif, porphyritic alkaline lamprophyre and alkali basalt dikes (basanite and tephrite compositions) present clinopyroxene and olivine antecrysts [37].

### 3. Materials and Methods

A systematic study of clinopyroxene and olivine compositional variations was developed for the different intrusions of the PN massif (sample points indicated in Figure 1C). Selected polished thin sections were the subject of detailed petrographic analysis by scanning electron microscopy (SEM) and energy-dispersive X-ray spectroscopy (EDS) yielding backscattered electron images and spectrograms. The analyses were conducted using a scanning electron microscope LEO 440I Microscope coupled with an Oxford Inca EDS system in the Department of Sedimentary and Environmental Geology (IGc-USP) Scanning Electron Microscopy Laboratory. Acceleration potential of 20 kV and beam current varying from 6.5 to 12.6 nA were applied throughout the analytical process. Electron microprobe analyses (EMP) were performed by wavelength-dispersive X-ray spectroscopy (WDS) using a JEOL JXA-8600 at the GeoAnalítica Core Facility of the Instituto de Geociências, University of São Paulo. The electron microprobe was equipped with five wavelength-dispersive spectrometers with the following pairs of analytical crystals **TAP**/**STE**, **TAP**/**PET**, **LIF**/**PET**, **PET**/**LIF** and **LIF**/**PET**, respectively (crystals in bold and underlined were those used in the routines of this study). Operating conditions were 15 kV for accelerating potential, 20 nA for probe current, and about 1–5 µm for beam diameter. Peak counting times ranged from 10 s for mostly major elements to 20 s for minor and trace elements. Silicate minerals and synthetic oxides were employed as standards (see Supplementary Materials A—Table SA1 for details of standards, spectral lines and other analytical parameters), with the data corrected on-line using the PROZA program [49]. Results and structural formulae are presented in the Supplementary Materials A (Tables SA2 and SA3). Structural formulae were calculated in accordance with [50,51]. Fe<sup>3+</sup>/Fe<sup>2+</sup> ratios were calculated by stoichiometry following the method of [52].

Seven samples that correspond to the most primitive lithologies of each intrusion of PN (compilation of whole-rock analyses of PN are offered in Supplementary Materials B) were selected for minor and trace element in situ analyses in clinopyroxene and olivine grains by laser ablation inductively coupled plasma mass spectrometry (LA-ICPMS). Trace element analyses by LA-ICPMS were performed at the Chemistry and ICP Laboratory of the GeoAnalítica-USP core facility. Analytical work utilized a Perkin Elmer ELAN 6100DRC ICP-MS instrument equipped with a New Wave UP 213 AF Laser Ablation with a super-cell chamber. Analytical procedures were performed according to [53]. Operating conditions were 0.2–0.3 mJ in the laser, about 60 µm for beam diameter (spot analyses) and an RF power of 1400 W. The analytical time was 120 s, with the first 60 s used as blank, and 8.3 s of integration time for each element. Synthetic glasses were employed as standards: BHVO-2G (USGS) for quantification and drift control, and the BIR-2G, BCR-2 and NIST-612 for quality controls (Supplementary Materials C and D). The following elements (with their respective masses) were analyzed for both clinopyroxene and olivine routines: Li<sup>7</sup>, P<sup>31</sup>, Sc<sup>45</sup>, Ti<sup>49</sup>, V<sup>51</sup>, Cr<sup>52</sup>, Mn<sup>55</sup>, Co<sup>59</sup>, Ni<sup>60</sup>, Cu<sup>65</sup>, Zn<sup>66</sup>, Ga<sup>71</sup>, Sr<sup>88</sup>, Y<sup>89</sup>, Zr<sup>90</sup>, Nb<sup>93</sup>, La<sup>139</sup>, Ce<sup>140</sup>, Pr<sup>141</sup>, Nd<sup>143</sup>, Sm<sup>147</sup>, Eu<sup>151</sup>, Gd<sup>155</sup>, Tb<sup>159</sup>, Dy<sup>163</sup>, Ho<sup>165</sup>, Er<sup>166</sup>, Tm<sup>169</sup>, Yb<sup>173</sup>, Lu<sup>175</sup>, Hf<sup>179</sup>, Ta<sup>181</sup>, Pb<sup>208</sup>, Th<sup>232</sup>, U<sup>238</sup>. For data integration and determination of concentrations, detection limits and analytical errors of the different elements, the Glitter 4.4.2 software [54] was used. As an internal standard for normalization and quantification purposes, CaO and MgO contents from the electron microprobe analyses were utilized for clinopyroxene and olivine, respectively. Linear adjustment was selected as the interpolation method for drift control and quantification. In the Supplementary Materials C and D, more than the concentrations (in ppm), the uncertainties (1σ) and minimum detection limits for each individual point are offered. Errors (1σ) are around 10% for mostly trace elements analyzed but are markedly above this range for the highly incompatible elements in olivine.

## 4. Results

### 4.1. Clinopyroxene and Olivine Paragenesis

Coarse-grained clinopyroxene (diopside cores and Ti-augite mantling and rims) and olivine primocrysts are the main cumulus phases of the CI, WI and NI and the main macrocrysts of the EI and SSI from PN (Figure 2). Clinopyroxene, the main mafic phase of the entire PN massif, evidences complex growth histories. These are indicated by (i) completely to partially resorbed diopside cores, with dissolution surfaces (including gulf texture) and mantled (growth type) by Ti-augite, by (ii) completely to partially resorbed diopside cores, with pervasive resorption and replaced by intercumulus minerals (Ti-augite, biotite, kaersutite, magnetite, plagioclase), by (iii) normal step zoning, by (iv) crystals with oscillatory zoning with coarse banding and with reverse zonings included, and by (v) sieve-textured crystals (Figure 3; Table 1). All these types of zoning and textures are suggestive of open-system processes [9,29,31,55,56]. Olivine is found as cumulus crystals, as minor inclusions in few diopside cores, and partially involved by Ti-augite rims in the most primitive rocks of the CI, WI and NI (Figures 2 and 3; Table 1). They present normal progressive zoning or occur as almost homogeneous crystals. In more evolved samples, olivine is absent or was completely resorbed. In EI, olivine is found as rounded macrocrysts presenting normal zoning and with resorption textures followed by pyroxene and biotite coronas. In SSI, olivine is also found as macrocrysts with normal progressive zoning and included in clinopyroxenite autoliths.

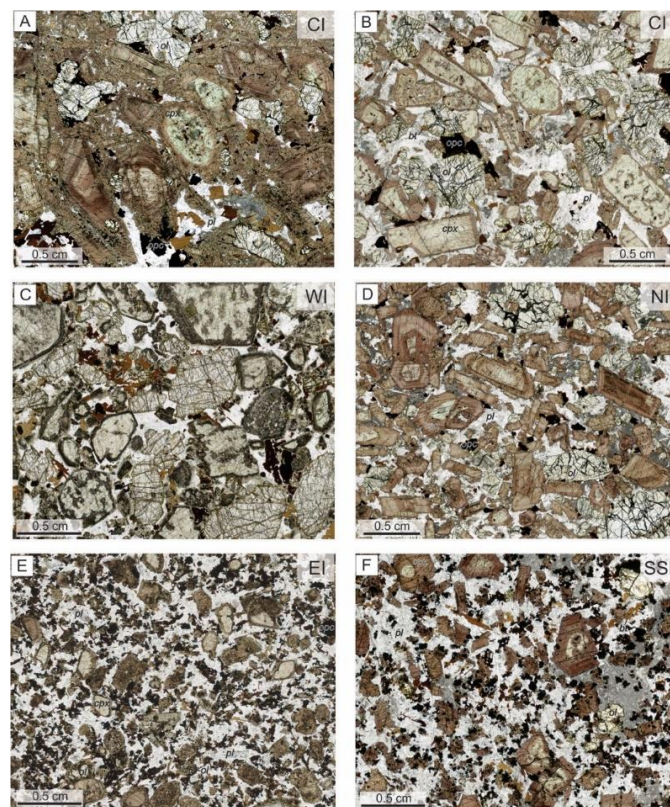


**Figure 2.** Petrographic aspects of the main intrusions of the Ponte Nova mafic–ultramafic alkaline massif in plan-polarized light. (A–D) Typical cumulate texture for the main cumulate intrusions, defined mainly by clinopyroxene and olivine primocrysts, with clinopyroxene as the main phase. (E,F) Porphyritic and inequigranular textures found in EI and SSI, with macrocryst population formed by clinopyroxene, subordinate olivine and minor plagioclase. Corrosion and sieve textures on complex step-zoned clinopyroxene cumulus crystals, with diopside relict cores (beige) and Ti-augite (brown) mantling and rims are found in all intrusions. Utilized mineral abbreviations: cpx, clinopyroxene; ol, olivine; opc, opaque minerals; pl, plagioclase; for additional abbreviations, see Figure 1.

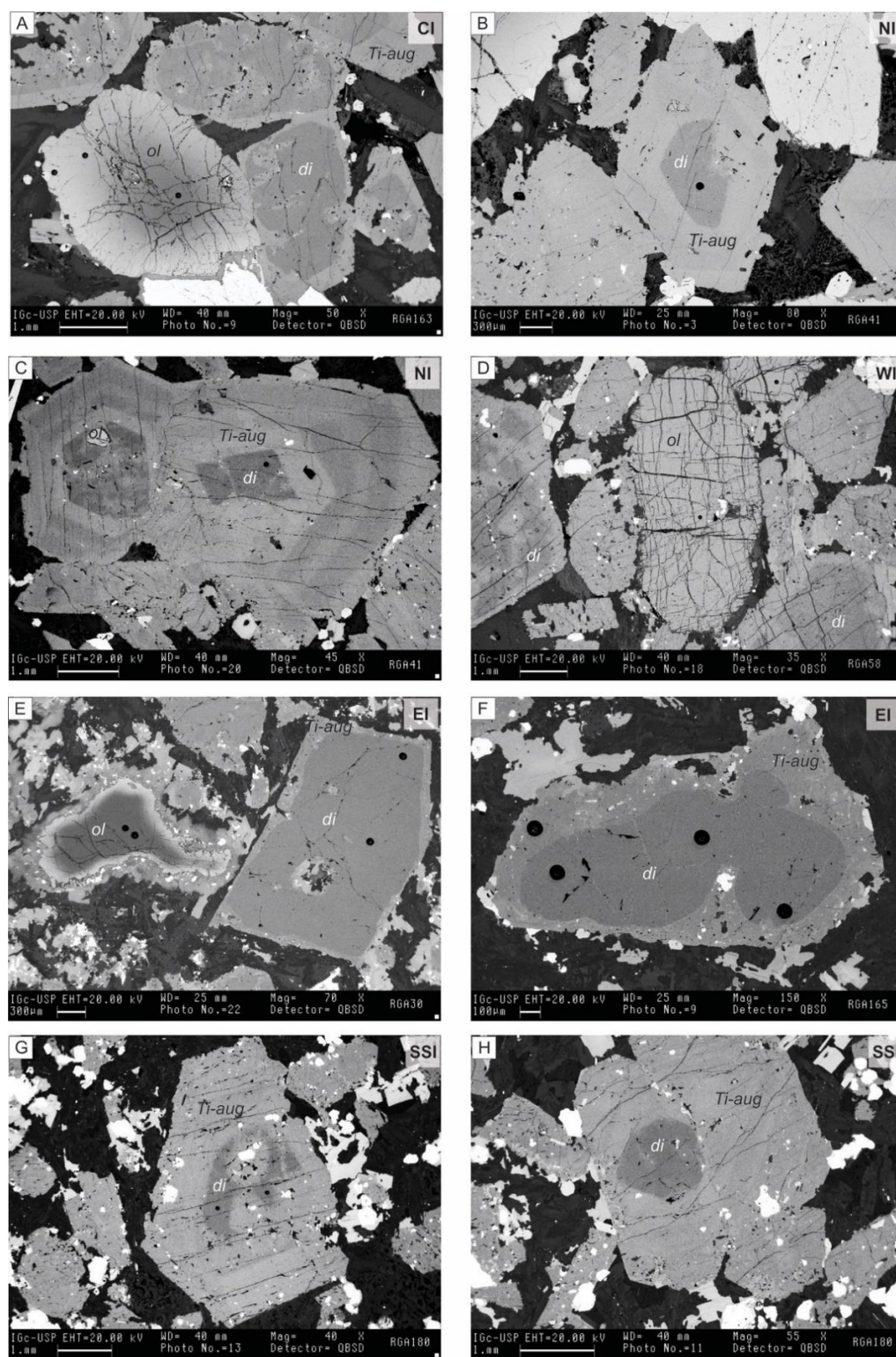


**Figure 3.** Backscattered electron images of clinopyroxene and olivine primocrysts of the Ponte Nova mafic-ultramafic alkaline massif. Relict cores of high-Mg diopside compositions are found in complex-zoned crystals of all intrusions (A–H). Mantling and rims of clinopyroxene crystals are mainly formed by Ti-augite (A–H). Mostly, the relict cores of diopside are partially corroded, presenting more rounded forms, typical of antecrysts. Zoned olivines with high-Mg cores are found mostly in CI (A) and EI (E), whereas typical cumulated olivines, as in WI (C) are almost unzoned. Utilized mineral abbreviations: di, diopside, ol, olivine; Ti-aug, titanite.

**Table 1.** Summary of clinopyroxene and olivine paragenesis in the main intrusions of the Ponte Nova mafic–ultramafic alkaline massif.

Intrusion	Lithologies	C.I.	Early Magmatic Phases (Primocrysts)	Clinopyroxene in the Most Primitive Samples		Olivines in the Most Primitive Samples	
				Crystal Types	Zoning and Textures	Crystal Types	Zoning and Textures
<b>CI (lower zone)</b>	(cumulatic) Ol clinopyroxenites, Ol-bearing clinopyroxenites, Ol melagabbros, Ol-bearing melagabbros	97–70	Di, Ti-Aug, Ol, $\pm$ Ti-Mgt, $\pm$ Ap, $\pm$ Pl	(1) zoned cumulus crystals	Completely to partially resorbed diopside cores (1) with dissolution surfaces (including gulf texture) and (growth) mantled by titanaugite and (2) with pervasive resorption and replaced by intercumulus minerals (Ti-aug, bt, krs, mgt, pl), (3) normal step zoning, (4) oscillatory zoning with coarse banding (reverse zonings included)	(1) cumulus crystals, (2) inclusions in diopside cores, (3) partially or totally involved by titanaugite rims	(1) normal progressive zoning, (2) normal step zoning
<b>WI (lower zone)</b>	(cumulatic) Ol melagabbros, Ol-bearing melagabbros, Ol-bearing clinopyroxenites	99–75	Di, Ti-Aug, Ol, $\pm$ Ti-Mgt, $\pm$ Ap, $\pm$ Pl	(1) zoned cumulus crystals		(1) cumulus crystals, (2) minor inclusions in few diopside cores, (3) partially involved by titanaugite rims	(1) normal progressive zoning
<b>NI (lower zone)</b>	(cumulatic) Ol melamonzogabbros, Ol-bearing melamonzogabbros	76–67	Di, Ti-Aug, Ol, $\pm$ Ti-Mgt, $\pm$ Ap, $\pm$ Pl	(1) zoned cumulus crystals		(1) cumulus crystals, (2) minor inclusions in few diopside cores, (3) partially involved by titanaugite rims	(1) normal progressive zoning, (2) normal step zoning (dirty cores, clean rims)
<b>EI (lower zone)</b>	(seriate to macrocrystic) Nph monzodiorites, Nph-bearing monzodiorites	58–51	Di, Ol, Pl, $\pm$ Ap	(1) zoned macrocrysts	Completely to partially resorbed diopside cores (1) with dissolution surfaces and mantled by titanaugite and (2) with pervasive resorption and replaced by intercumulus minerals (Ti-aug, bt, krs, mgt, pl), (3) normal step zoning, (4) sieve texture	(1) rounded macrocrysts	(1) normal step zoning, (2) resorption, with biotite coronas
<b>SSI</b>	(macrocrystic) Nph-bearing melamonzogabbros	67	Di, Ti-Aug, Ol	(1) zoned macrocrysts	Completely to partially resorbed diopside cores (1) with dissolution surfaces and mantled by titanaugite and (2) with pervasive resorption and replaced by intercumulus minerals (Ti-aug, bt, krs, mgt, pl), (3) normal step zoning, (4) included in cumulatic clinopyroxenitic autoliths	(1) macrocrysts (2) included in clinopyroxenitic cumulate autoliths	(1) normal progressive zoning

## 4.2. Mineral Chemistry

### 4.2.1. Major Elements

**Clinopyroxene.** Clinopyroxene crystals from different intrusions of the PN are mainly within the range  $Wo_{39-47}En_{34-48}Ae_{0-5}$ , and chemically classified as diopside.  $Mg\#_{cpx}$  [ $Mg/(Mg + Fe_T)$ , molecular proportions] varies in the range of 0.69–0.90, with the highest values related to the cores of crystals from the most primitive samples of each intrusion. The  $Mg\#_{cpx}$  is positively correlated with  $Cr_2O_3$  (0–1.3 mass%) and negatively correlated with  $Al_2O_3$  (2.0–9.9 mass%),  $TiO_2$  (0.5–4.5 mass%) and  $Na_2O$  (0.2–1.2 mass%) (Figure 4). The relict cores present higher  $Mg\#$  (mostly 0.85–0.90 to the cumulate intrusions and 0.80–0.86 to the porphyritic intrusions), Cr and lower Ti, Na and Al than Ti-augite mantling and rims. The clinopyroxene compositions indicate main substitutions of diopside for hedenbergite (Hd) and diopside for the main Ca-tschermak endmembers ( $Ca^{VI}Al^{IV}AlSiO_6$ ,  $CaTiAl_2O_6$  and  $CaFe^{3+}AlSiO_6$ ; Figure 5A). Especially for mantling and rims, the progressive increment of the CaTi-tschermak component is indicated by a positive correlation of  $^{IV}Al$  with  $Ti^{4+}$  of the M1 site (Figure 5B).

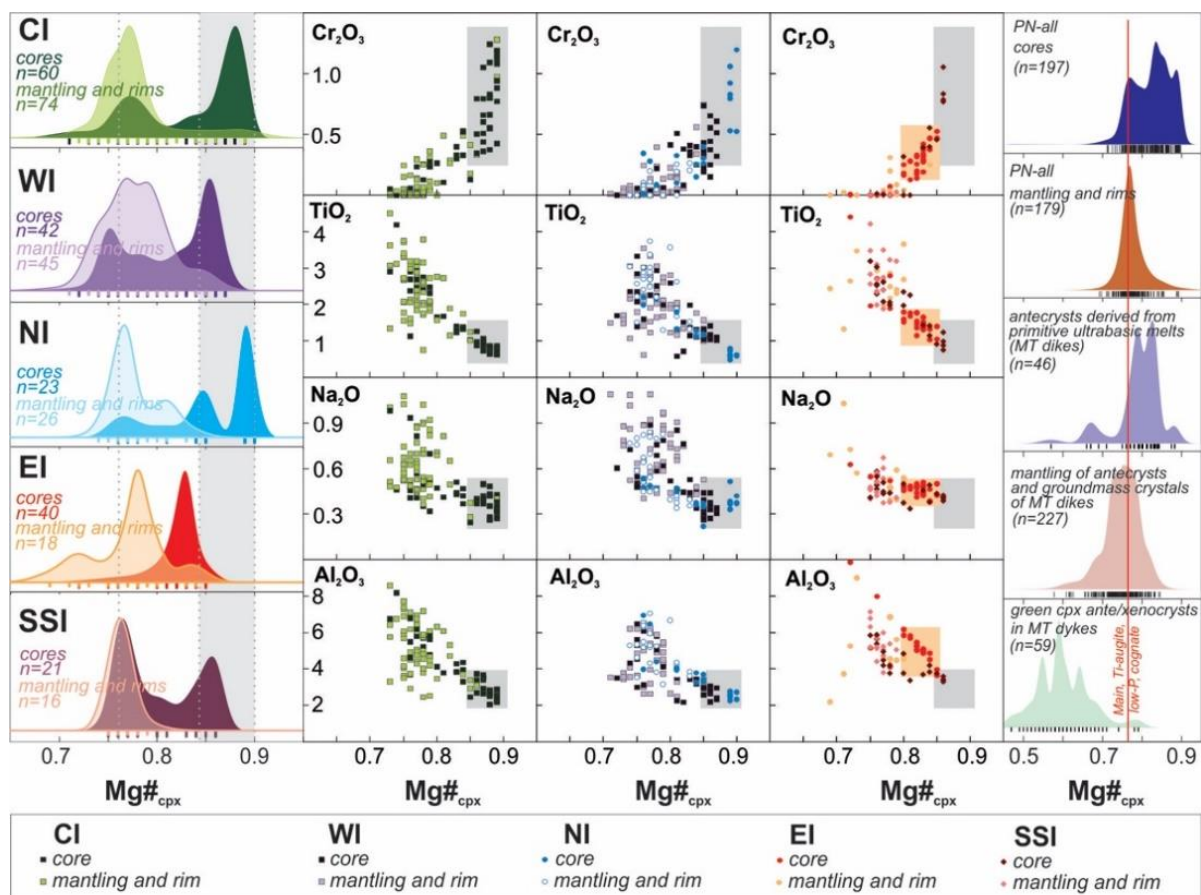


**Figure 4.** Clinopyroxene compositions of the Ponte Nova mafic–ultramafic alkaline massif. Kernel density estimates (KDEs; bandwidth = 0.01) of clinopyroxene  $Mg\#$  distribution for each main intrusion of the massif indicate one peak of lower  $Mg\#$  more compatible with Ti-augite compositions (gray dashed line) and one peak with higher  $Mg\#$  compatible with diopside relict cores (gray bar). Interestingly, the KDE of  $Mg\#_{cpx}$  for PN antecrysts are very similar to that found for antecrysts from the nearby Mantiqueira Range lamprophyre and alkali basalt dikes, as well as the KDEs for PN mantling and rims are very similar to that found for Ti-augite mantling, rims and matrix crystals for the cited nearby dikes.

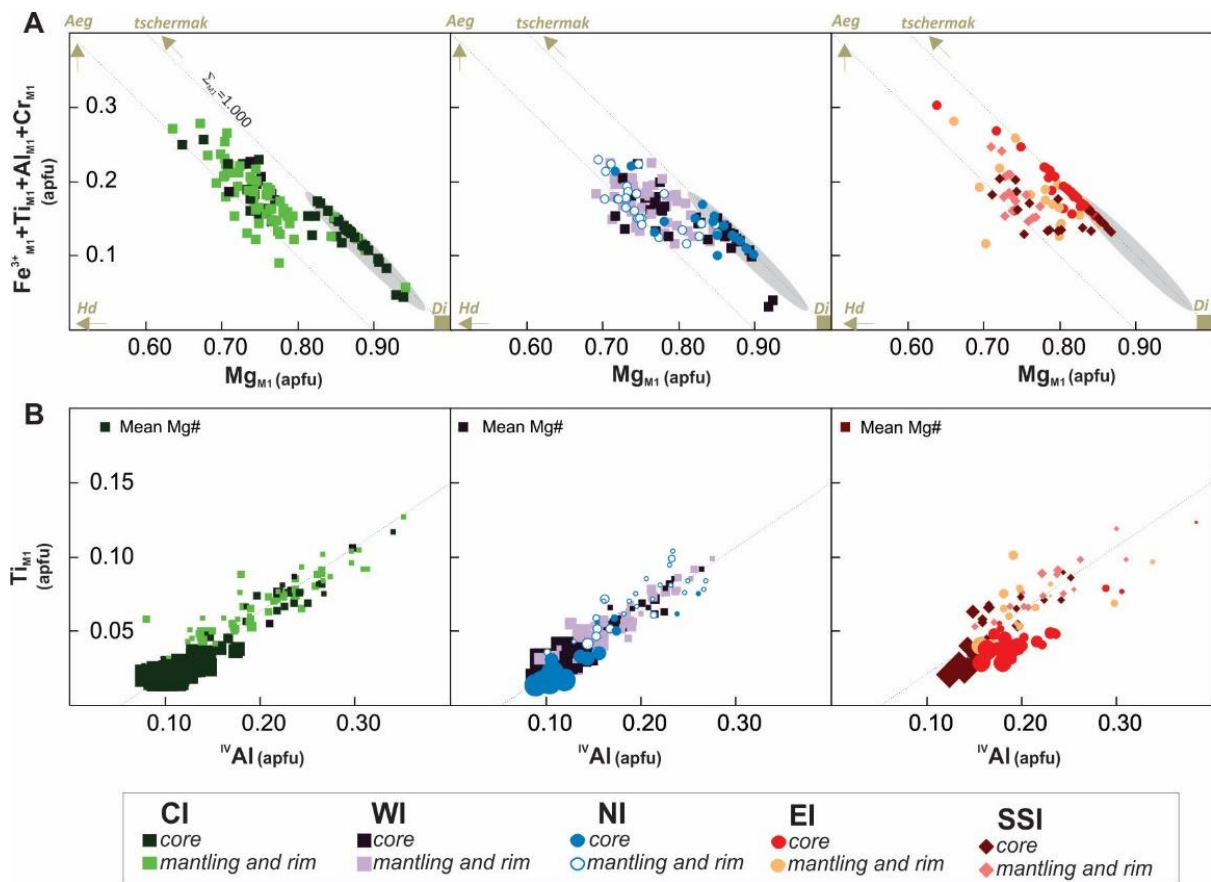


**Figure 5.** Clinopyroxene compositions of the Ponte Nova mafic-ultramafic alkaline massif. (A)  $Mg_{M1}$  vs  $Fe^{3+} + Ti_{M1} + Al_{M1} + Cr_{M1}$ , shows the main solid solution endmembers of these crystals and favoring substitutions of diopside(Di) with hedenbergite(Hd) and with the main Ca-tschermak endmembers ( $Ca^{VI}Al^{IV}AlSiO_6$ ,  $CaTiAl_2O_6$  and  $CaFe^{3+}AlSiO_6$ ). In (B), the importance of CaTiTs component is emphasized in the positive correlation of  $^{IV}Al$  in the tetrahedral site with  $Ti^{4+}$  in the M1 site. A third component qualitatively indicated in this graph is the  $Mg\#_{cpx}$ , which can be evaluated based on the symbol size (higher  $Mg\#$ , bigger symbols).

*Olivine.* Olivine crystals from the different intrusions of the PN are within the range of  $Fo_{86}$ – $Fo_{51}$ , with crystal cores from EI and CI presenting the highest values ( $Fo > 80$  mol.%) and crystals from CP and WI having the lowest ones ( $Fo < 56$  mol.%, mainly rims) (Figure 6). Positive correlation is found between  $Fo$  and NiO (0–0.31 mass%) and negative correlation is found between  $Fo$  and MnO (0.14–1.14 mass%). CaO (0.01–0.67 mass%) does not present clear linear correlation with  $Fo$  although a tendency of higher CaO values for crystal cores with higher  $Fo$  is observed. Two olivine groups are identified: (i) one associated with almost unzoned, cumulatic olivine crystals, with  $Mg\#_{ol}$  [ $Mg/(Mg + Fe_T)$ , molecular proportions] below 0.77, and (ii) another group is found for zoned olivine crystals with  $Mg\#_{ol} > 0.80$  (gray bar in Figure 6).

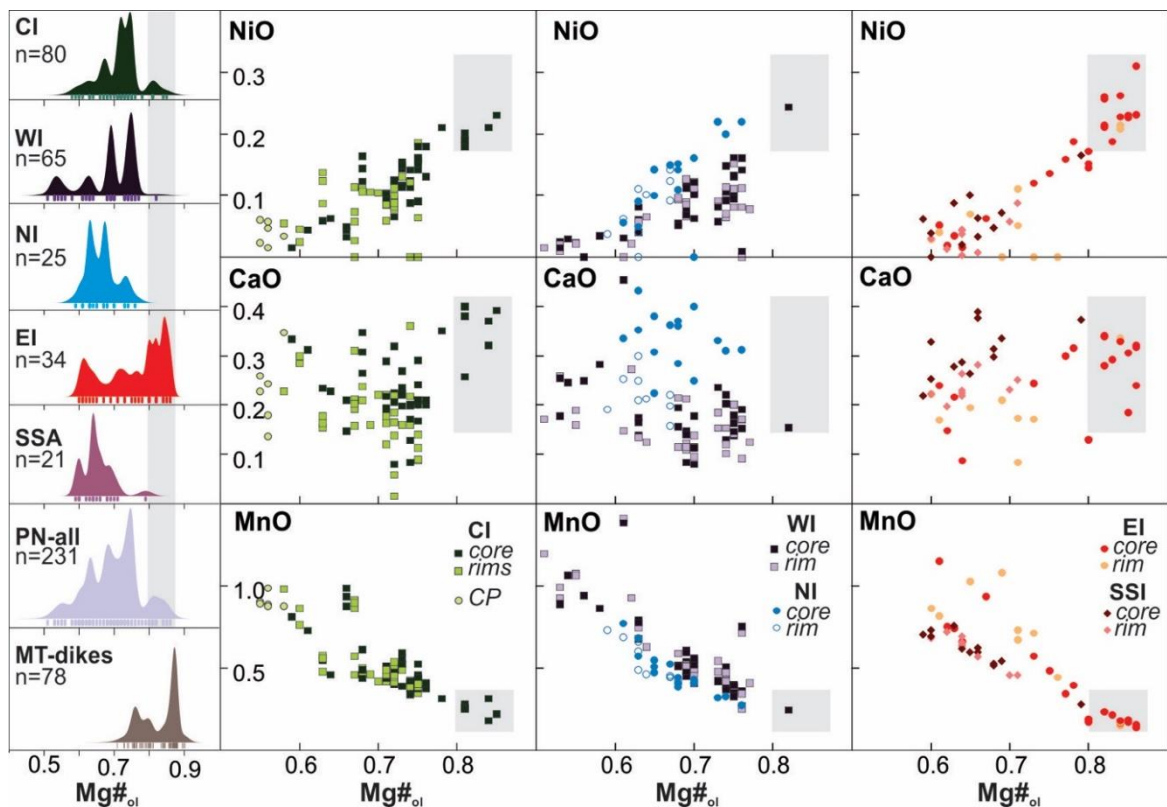


**Figure 6.** Olivine compositions of the Ponte Nova mafic–ultramafic alkaline massif. Kernel density estimates (KDEs; bandwidth = 0.01) of olivine Mg# distribution for each of the main intrusion of the massif. Interestingly, the main cluster is associated with almost unzoned, cumulative olivine crystals, with Mg# below 0.77. Another group (gray bar) is found for zoned olivine crystals with Mg# > 0.8. Zoned olivines are similar to the main group found for antecrysts in the Mantiqueira Range dikes (MT-dikes).

#### 4.2.2. Trace Elements

*Clinopyroxenes.* Trace element compositions were mainly determined in pyroxene crystals from the most primitive samples of the PN intrusions (Table SC2; Supplementary Material C). In general, diopside cores (Mg#<sub>cpx</sub> 80–90) have higher concentration of Ni (192–304 ppm) and lower values of V (108–335 ppm), Sr (75–131 ppm), Zr (9–56 ppm), Zn (15–26 ppm), Y (4–12 ppm), Hf (0.32–3.02 ppm) and REE (18–48 ppm) than Ti-augite mantling and rims (Mg#<sub>cpx</sub> = 0.69–0.84; Ni = 32–276 ppm; V = 197–573 ppm; Sr = 99–255 ppm; Zr = 59–1091 ppm; Y = 11–138 ppm; Hf = 2–38 ppm; REE = 46–821 ppm) (Table 2). Similar intervals for cores and rims are found for Sc (31–116 ppm) and Co (27–49 ppm).

Regarding chondrite-normalized [57] rare-earth element (REE) distribution patterns of clinopyroxenes from the PN (Figure 7), relict cores of each intrusion present contrasting compositions; marked lower values in the relict cores when compared to those from mantling and rims (Figure 7; WI mantling and rims were not analyzed due to the extensive exsolution features presented in those crystals). All chondrite-normalized REE distribution patterns display smooth LREE/HREE fractionation and exhibit a concave downward pattern for normalized LREEs, with slightly depleted La values relative to Ce and Pr values, and a negative slope for normalized HREEs ( $Gd_N/Yb_N > 2.5$ ). The compositions of some Ti-augite rims present an Eu-negative anomaly, suggesting a protracted crystallization of clinopyroxene, with its final stage just occurring after extensive fractionation of plagioclase. Whole-rock compositions (compiled from [41]—Supplementary Materials B) from the same units from which crystals were analyzed, present values of REE much more enriched than diopside cores (Figure 7). The relict cores found in the most primitive samples of each intrusion (all with resorption/corrosion features) present an evolution trend, the most

primitive found for CI and NI (richer in  $Mg\#_{\text{Cpx}}$ , Cr, Ni) and the most evolved related to EI (richer in Ti, Al, Na, Zn, Zr, REE, V, Co) (Figures 4 and 7). This trend seems to be independent of that found for the mantling and rims of each intrusion, which present an important overlap for most element (Supplementary Materials E).

**Table 2.** Summary of compositional ranges for trace element analysis on clinopyroxenes from the Ponte Nova massif.  $Mg\# = [Mg/(Mg + Fe_T)]$ , cationic proportions]. Individual analysis can be accessed in the Supplementary Materials.

	CI		WI		NI		EI		SSI									
	Relict Cores	Mantling and Rims	Relict Cores	Relict Cores	Mantling and Rims	Relict Cores	Mantling and Rims	Relict Cores	Mantling and Rims									
	n = 22	n = 10	n = 6	n = 10	n = 13	n = 31	n = 10	n = 9	n = 12									
	Min	Max	Min	Max	Min	Max	Min	Max	Min	Max	Min	Max	Min	Max	Min	Max	Min	Max
Mg#	0.85	0.89	0.75	0.84	0.85	0.87	0.85	0.90	0.76	0.81	0.80	0.85	0.69	0.84	0.84	0.86	0.74	0.78
Ti	3409	6553	8471	19016	5693	7920	3291	6092	9461	16630	7165	13828	6648	16519	5026	8476	10810	22386
Cr	1017	8257	32	2105	1473	3779	1932	9310	54	2311	483	3355	18	1361	2388	6090	18	1366
Ni	214	280	121	276	217	256	237	304	142	226	192	274	32	123	193	271	62	221
Co	27.1	38.2	34.8	48.3	32.5	38.3	30.1	37.2	36.7	49.2	34.4	45.8	26.6	39.2	34.3	37.0	32.0	44.4
Sr	75.5	109	116	159	107	131	77.3	94.4	106	186	84.3	106	98.5	218	100	127	126	255
Y	4.29	10.0	14.2	62.1	5.99	8.36	4.18	6.76	13.5	82.3	7.82	11.8	11.4	74.5	8.49	10.5	11.9	138
Zr	9.6	34.2	65.8	325	14.4	23.8	9.12	23.2	62.6	639	25.5	55.7	63.1	374	16.7	34.4	59.3	1091
Hf	0.46	1.66	2.23	11.0	0.85	1.31	0.32	1.04	2.58	15.9	1.27	3.02	3.70	11.6	0.96	1.74	3.20	37.5
Zn	14.6	24.4	38.4	64.6	18.8	24.2	17.4	22.6	39.2	63.8	18.2	25.8	22.7	82.5	20.9	24.2	29.5	92.0
V	108	203	340	537	146	193	120	188	350	544	223	335	197	317	171	238	293	573
Sc	54.5	84.6	47.1	98.7	69.1	85.3	46.2	78.9	31.1	81.4	73.2	93.4	40.5	108	65.1	83.7	51.7	116
La	1.82	3.10	5.53	33.3	1.87	2.46	1.27	2.20	4.25	55.3	2.08	3.32	3.22	51.6	2.23	3.31	4.65	80.9
Ce	5.28	11.6	19.2	127	7.60	10.5	5.40	8.58	19.9	200	7.48	12.5	11.6	154	8.76	13.4	21.5	278
Pr	1.03	2.07	3.25	20.1	1.55	2.09	0.92	1.63	3.15	27.7	1.43	2.42	2.26	22.4	1.73	2.61	4.01	47.2
Nd	5.29	10.7	15.7	86.0	9.05	12.3	4.94	8.44	16.2	108	8.25	13.9	12.8	94.7	9.73	14.7	20.5	236
Sm	1.35	3.18	3.88	20.7	2.50	3.65	1.45	2.50	3.79	23.3	2.52	4.00	4.19	23.0	2.92	3.96	5.33	50.8
Eu	0.52	1.19	1.36	5.07	0.89	1.17	0.48	0.85	1.40	5.16	0.79	1.42	1.33	5.58	0.93	1.31	1.78	7.52
Gd	1.28	3.46	3.64	18.1	2.37	3.29	1.22	2.25	4.64	25.0	2.56	4.13	4.44	22.1	2.73	3.79	4.37	42.1
Tb	0.21	0.45	0.69	2.69	0.29	0.38	0.16	0.30	0.64	3.60	0.34	0.60	0.56	2.72	0.37	0.53	0.63	6.53
Dy	0.95	2.56	3.58	13.7	1.47	2.25	1.01	1.61	2.95	20.2	1.88	3.16	2.85	15.5	1.97	2.82	3.16	39.7
Ho	0.16	0.38	0.507	2.40	0.23	0.38	0.18	0.30	0.49	3.37	0.32	0.51	0.46	2.80	0.31	0.45	0.56	5.43
Er	0.36	0.89	1.16	6.17	0.45	0.72	0.43	0.62	1.19	9.41	0.70	1.13	1.02	6.50	0.71	1.07	1.12	13.3
Tm	0.03	0.14	0.13	0.76	0.05	0.11	0.05	0.07	0.10	1.19	0.07	0.15	0.14	0.89	0.08	0.13	0.12	1.80
Yb	0.18	0.54	1.01	4.13	0.21	0.45	0.25	0.44	0.54	5.93	0.43	0.61	0.62	8.26	0.40	0.69	0.77	9.25
Lu	0.03	0.09	0.05	0.66	0.03	0.07	0.03	0.06	0.07	0.75	0.05	0.09	0.09	0.87	0.04	0.09	0.09	1.49
ΣREE	19.9	39.7	59.7	341	29.3	39.3	18.1	29.9	62.4	487	29.4	47.9	45.6	408	33.0	48.2	68.5	821

*Olivines.* Trace element compositions were mainly determined in olivine crystals from the most primitive samples of the PN intrusions (mainly cores;  $Fo_{65-86}$ ) (Supplementary Material D). Higher concentrations were found for Co (146 a 249 ppm), Zn (99 a 347 ppm), Ti (58–190 ppm), Cr (4–382 ppm), P (21–158 ppm) and Li (0.2–12 ppm). Restricted values were found for V (1.7–7.9 ppm) and Sc (2.8–7 ppm). Actinides (U + Th + Pb) and REE do not represent more than 1 ppm, nor do other analyzed elements such as Ta and Hf. The crystal cores with higher Fo (>80) also have higher Cr and Sc and lower Zn.

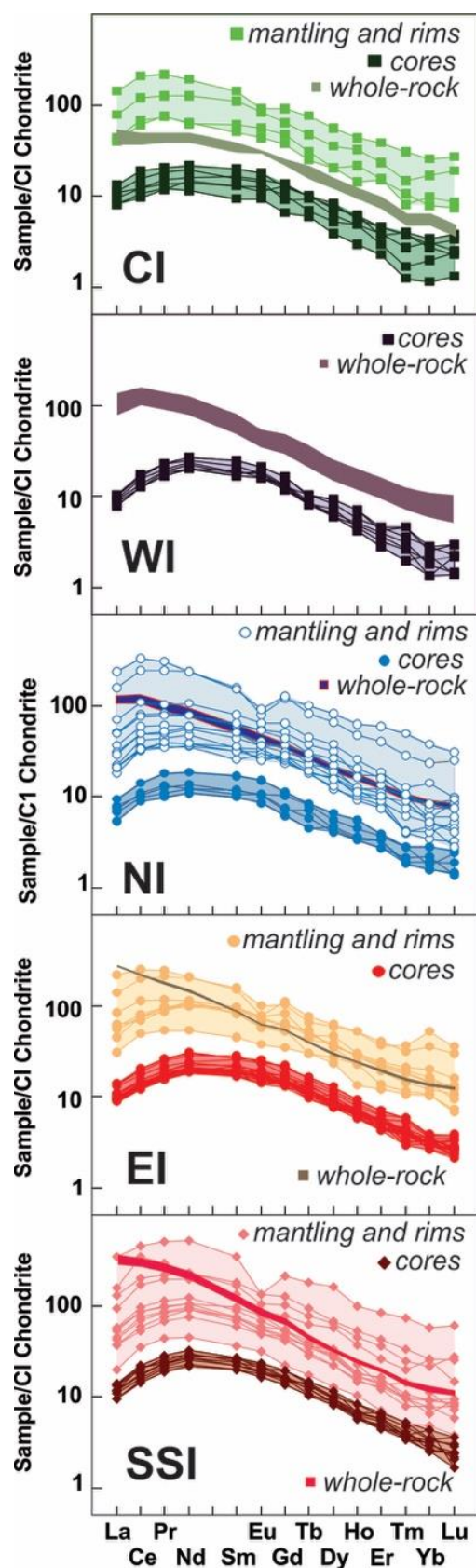


Figure 7. Chondrite-normalized (McDonough and Sun, 1995) [57] REE distribution diagram of clinopyroxenes from the Ponte Nova mafic–ultramafic alkaline massif. Fields of whole-rock compositions were made after compilation from Azzone et al. (2016; 2020—see Supplementary Material B) [41,48].

## 5. Discussion

### 5.1. Antecrysts in the Ponte Nova Massif

The presence of complex zoned microstructures, with diopside cores and Ti-augite mantling and rims exhibiting significant compositional differences, indicates that almost no subsolidus diffusive exchange occurred in most of the selected clinopyroxene crystals [58,59]. This is not the case of most of the analyzed olivine, especially those that present almost homogeneous compositions. In fact, the samples that presented only few clinopyroxene crystals with partially corroded cores (with most of all re-equilibrated to Ti-augite compositions) are the same where olivine crystals are almost homogeneous. Thus, the relict cores of clinopyroxene crystals and of zoned olivines, both found in the most primitive samples of each intrusion, can give some clues to a complex plumbing system existing beneath the PN massif [31,55,56,60–62]. To establish if clinopyroxene or olivine was the first mineral to be crystallized from the studied plumbing system, the Mg–Fe exchange coefficient [ $Kd_{Mg-Fe}^{cpx-ol} = (X_{Mg}^{cpx} \times X_{Fe}^{ol}) / (X_{Fe}^{cpx} \times X_{Mg}^{ol})$ ] between these primocrysts from different samples of PN massif was calculated. Following experimental data in similar chemical systems, a  $Kd_{Mg-Fe}^{cpx-ol}$  range of 1.04–1.91 tends to represent crystallization in equilibrium conditions [63]. The  $Kd_{Mg-Fe}^{cpx-ol}$  values indicate that most of the high-Mg clinopyroxene relict cores are more primitive than the homogeneous olivine crystals, being instead in equilibrium with cores of strongly zoned olivine crystals (Figure 8).

These primitive diopside cores and their restricted evolution trend (Figure 4) imply the existence of a deeper magmatic chamber that could be connected to the shallow magmatic reservoir represented by the PN massif, in a complex plumbing system [3,30,64]. These relict cores can be classified as antecrysts, crystals that did not crystallize directly from the host magma in which they are contained, although they maintain a genetic relationship with the same system [3,10,29]. In fact, the diopside relict cores and the high-Mg zoned and corroded olivine crystals are both similar in composition, respectively, to the high-Mg clinopyroxene and olivine antecrysts from the lamprophyres and alkali basalt dikes from the nearby Mantiqueira Range [37] (Figure 8A). Otherwise, PN Ti-augite mantling and rims are in compositional equilibrium with the nearly homogeneous olivines (Figure 8B). Possibly, olivines with lower Mg# than that of equilibrium compositions with the clinopyroxene are affected by faster Fe–Mg diffusive exchange between olivine and liquid. The Ti-augite mantling and rims are similar in composition to the phenocrystic and groundmass Ti-augite from the lamprophyres and alkali basalt dikes from the nearby Mantiqueira Range. These similarities allow the assignment of the primitive dikes from the Mantiqueira Range [37,38] as possible liquid counterparts of the PN cumulates (Figure 8). The presence of these antecrysts suggests a hidden deeper magmatic chamber, and understanding this part of the plumbing system responsible for the trans-crustal evolution of PN alkaline magmas and estimating the intensive parameters involved (such as P and T) are fundamental.

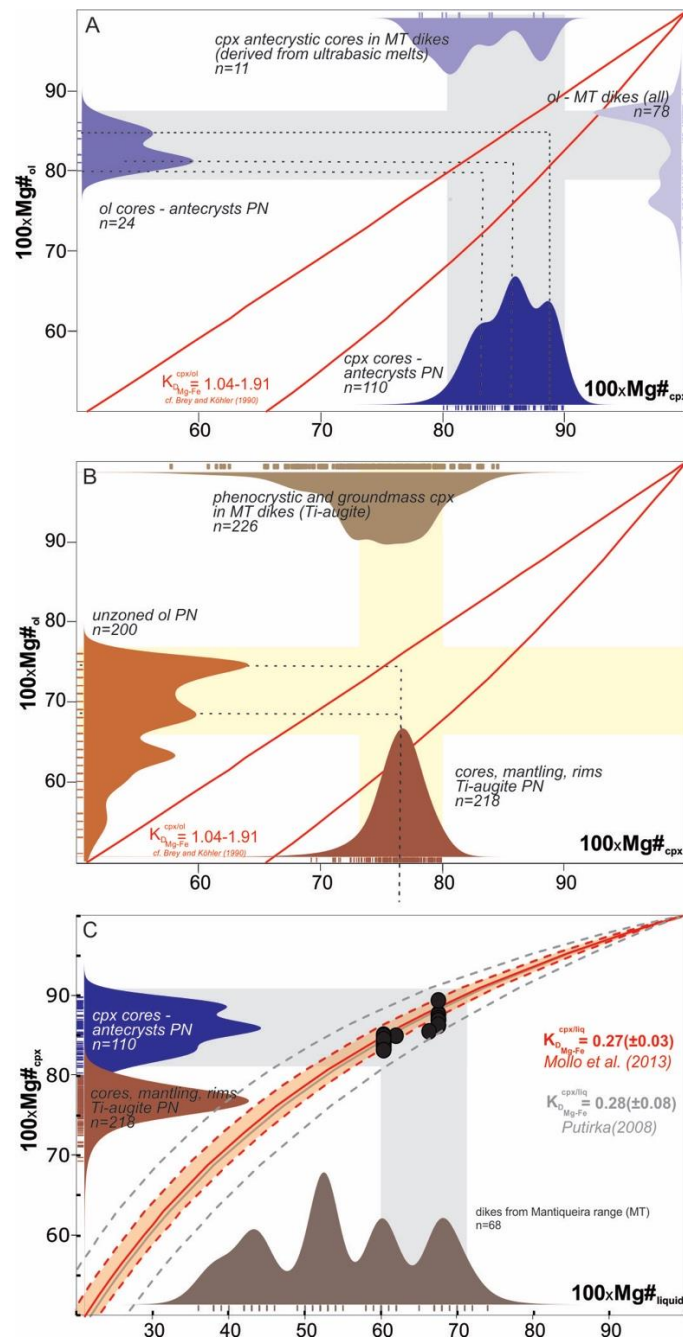


**Figure 8.** Mg–Fe equilibrium exchange between clinopyroxene and olivine from PN and liquids from Mantiqueira Range (compiled data from [37]). (A,B) KDEs of  $Mg\#_{cpx}$  vs. KDEs of  $Mg\#_{ol}$  are compared with the curves of Mg–Fe exchange calculated using experimentally determined coefficients ( $K_D^{Cpx-Liq}$ ) ranging from 1.04–1.91 ([63]), and believed to represent crystallization in equilibrium conditions. (C) Mineral–melt equilibrium diagram with KDE of the  $Mg\#_{cpx}$  of the PN with the KDE of  $Mg\#$  of alkaline dikes from the Mantiqueira Range [38], attributed to potential liquids from which cumulates were formed [ $Mg\#_{liquid} = Mg/(Mg + Fe^{2+})$ , molecular proportions and using  $Fe^{2+}/\Sigma Fe = 0.85$ ]. The curves represent the range in which mineral and melt compositions are in equilibrium based on iron–magnesium exchange [65]. Iron–magnesium coefficients are from compilation of [66] and [67] for clinopyroxene–liquid exchanges. Based on (C), the high-Mg diopside relict cores are in equilibrium with the high-Mg liquids ( $Mg\# > 60$ ) of the Mantiqueira Range, whereas the most common Ti-augite and unzoned olivines are mostly in equilibrium with dike compositions with  $45 < Mg\# < 50$ . The points plotted in graph are the pairs of clinopyroxene–liquid which attended to the filters of equilibrium conditions for the application of the geothermobarometer of [68].

### 5.2. Estimation of Intensive Parameters (P-T) for High-Mg Diopside Antecrysts of PN

To estimate the crystallization pressure and temperature of the clinopyroxene antecrysts of PN, we apply the thermobarometers of [66,68]. The thermometer is based on the temperature sensitivity related to the equilibrium exchange between the diopside + hedenbergite [Ca (Mg, Fe)-DiHd]-liquid and jadeite (NaAlSi<sub>2</sub>O<sub>6</sub>-Jd)-liquid [66,69] and it is also based on the strong pressure dependency for the introduction of jadeite into clinopyroxene in equilibrium with the liquid, where a high Jd component would occur at high pressures [68,69]. Both equations are co-dependent and corresponding to thermodynamic expressions calibrated from experimental database that include tholeiitic and alkaline compositions in hydrous systems, with SEE (equivalent to the standard deviation- $\sigma$ ) of 1.4 kbar and 45 °C for pressure and temperature, respectively [66,68,69].

For their application, the authors of [68] recommend looking for putative liquids that are in equilibrium with the clinopyroxene compositions. In this case, we choose the ultrabasic alkaline dikes of the Mantiqueira Range [37,38] that outcrop in the region. The clinopyroxene relict cores and some of the most primitive liquid (dikes) compositions of this area are inside of the experimental data range used for model calibration by [68] and, therefore, suitable for the application of this barometer. Moreover, the [66] thermometer is the most suitable for hydrous systems [66,68].

We took into consideration the following compositional filters in our database, in part according to [68]: (i) clinopyroxene relict core compositions with Mg#<sub>cpx</sub> > 0.80 and cation sums between 3.96 and 4.04, with 1% of uncertainty of the theoretical value of 4; (ii) clinopyroxene Jd-component > 0.01; (iii) clinopyroxene with Al cation > 0.11; and (iv) mass of LOI < 4.5% and Mg#<sub>liq</sub> > 60 from whole-rock analysis of Mantiqueira dikes.

The clinopyroxene relict core–liquid (dikes) pairs were also filtered according to equilibrium constant ( $K_D$ ) and multicomponent equilibrium, as suggested by [67,70]. The  $K_{D_{Fe-Mg}}^{Cpx-Liq}$  filter compares values calculated with Equation (35) from [66] and the Equation from [65], accepting a  $\Delta K_D < 0.03$ , consistent with the uncertainty of  $K_D$  value reported by Mollo et al. (2013;  $K_D = 0.27 \pm 0.03$ , Figure 8C). The multicomponent equilibrium filter compares the predicted (theoretical calculated) and the observed clinopyroxene components, accepting values within the reported SEE error of  $\pm 0.06$  for  $\Delta DiHd$ ,  $\pm 0.05$  for  $\Delta EnFs$ , and  $\pm 0.03$  for  $\Delta CaTs$  [67,71] for the predicted values. These filters improve the equilibrium condition that must exist in the selected crystal–liquid pairs [67,70].

Applying the filters, we obtained 28 pairs of clinopyroxene relict core–liquid, using three putative liquids from Mantiqueira Range, and with clinopyroxene compositions of all studied intrusions being represented (Supplementary Material F). Despite the individual values, a Kernel density estimation (KDE) diagram was applied (Figure 9). The peak determinations of the KDEs indicate a T of  $1166 \pm 45$  °C and a P of  $5.6 \pm 1.4$  kbar for the crystallization conditions in the hidden chamber of PN (Figure 9). Six clinopyroxene relict core–liquid pairs present lower pressures (<4 kbar, Figure 9), far from the main peak of ~5.6 kbar. These values are interpreted as a possible consequence of re-equilibrium between the clinopyroxene relict core and the surrounding liquid. Excluding these six pairs from the previous set, the peak of KDE is ~1173 °C and 5.8 kbar. The weighted mean values of P and T considering the uncertainties of 22 pairs are  $5.7 \pm 0.30$  kbar (MSWD = 0.3) and  $1171 \pm 10$  °C (MSWD = 0.13), respectively. All the PN intrusions are included in the 22 clinopyroxene relict core–liquid pairs and the obtained individual values for P are similar and within the uncertainties; thus, a common magmatic chamber for the formation of these clinopyroxene and olivine antecrysts is indicated. Additionally, we tested the equilibrium conditions of clinopyroxene antecryst cores found in primitive alkali basalts and lamprophyre dikes from the Mantiqueira Range: in a set of 11 analyses, just one clinopyroxene–liquid pair met the condition of the multicomponent equilibrium filters from [70] discussed above (Supplementary Material F). The resulting calculation of this pair indicate a P of  $6.9 \pm 1.4$  kbar and T of  $1180 \pm 45$  °C, which is completely similar to the values found for PN when the uncertainties are considered.

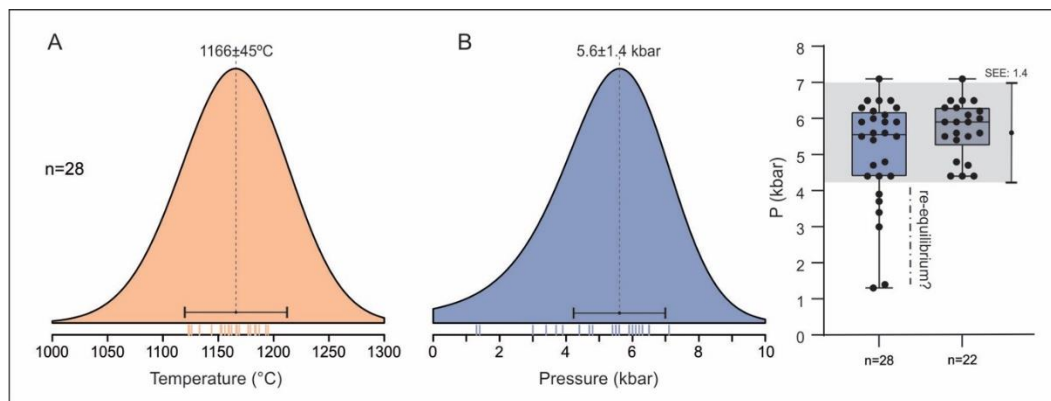


**Figure 9.** KDEs of temperatures and pressures calculated for the clinopyroxene antecrysts from PN using equations [66,68]. (A) Temperature KDEs is calculated with a bandwidth of 45 °C, as recommended in [66], with peak of estimations close to ~1180 °C. (B) Pressure KDEs is calculated with a bandwidth of 1.4 kbar, which is comparable to the SEE (1 $\sigma$ ) of [68] barometer, with peak of estimations of pressure of ~5.6 kbar, accompanied by boxplot graph. Considering just the antecrysts with minimum re-equilibrium (n = 22), the peak of P is ~5.8 kbar, values also consistent with the medians obtained using boxplot graph.

Mantling and rims of clinopyroxenes represent the more differentiate compositions from PN (i.e., <Mg#, >Al<sub>2</sub>O<sub>3</sub>, >TiO<sub>2</sub> and >Na<sub>2</sub>O), so the application of these thermobarometers is not recommended, will most of the data falling outside the proposed equilibrium filters. This indicates that the clinopyroxene sectors would be in disequilibrium crystallization with the host liquid, as attested by complex, oscillatory, and step zonings patterns found in these clinopyroxenes (Figures 2 and 3). The high TiO<sub>2</sub> content (up to 4.50 mass%) and high Ca-Tschermak's components (i.e., Ca<sup>VI</sup>Al<sup>IV</sup>AlSiO<sub>6</sub>, CaTiAl<sub>2</sub>O<sub>6</sub> and CaFe<sup>3+</sup>AlSiO<sub>6</sub>; 3–14 mol.%) in the mantling and rims sectors are outside the compositional calibration range used for the [68] barometer.

Although a quantitative determination of P estimates is not possible for the Ti-augite mantling and rim composition, their evolution trend suggests very low-P crystallization conditions (cf., [64,72–75]). Ti-augite from all intrusions of PN presents a very positive correlation of Ti and the <sup>IV</sup>Al (Figure 5) [74] showed that there are compositional differences between high and low pressure clinopyroxenes based on trends of increasing Ti and <sup>IV</sup>Al at the expense of silica, the increase in the <sup>IV</sup>Al/<sup>VI</sup>Al ratio and the increase in TiO<sub>2</sub> coupled with decreasing Mg#<sub>cpx</sub>. All these features are found for the PN clinopyroxenes. The experimental work of [75] with mildly alkaline lava also indicate that Ti and Al substitution and the proportion in which it occurs are very sensitive to pressure conditions. The comparison of PN clinopyroxenes with [75] experimental data suggests that high-Mg# relict cores were crystallized in different conditions from Ti-augites mantling and rims and that Ti-augite was formed in low-pressure environment due to their trend following lower Ti:Al proportions (Figure 10). [76] also point that the coupled increase in Ti in the M1-site and Al in the T-site is a main trend controlled by the progressive decrease in pressure. Following the procedure of [77], the PN mantling and rims present high calculated values of cell volumes (V<sub>CELL</sub> = 438.9–442.0 Å<sup>3</sup>; V<sub>M1</sub> = 11.6–11.9 Å<sup>3</sup>), pointing to very-low crystallization pressure [77], similar to some nearby Brazilian alkaline complexes [42,78–81]. In fact, the estimation of low-pressure conditions for the PN massif is consistent with the expected denudation estimates based on apatite fission track in the Precambrian rocks of Mantiqueira Range [82]. The exhumation through denudation of the Mantiqueira Range, associated with continental rifts developed since Early Cretaceous period, would not expose on the surface rocks generated under pressure above ~1 kbar [82–84]. Hence, in the studied plumbing system, Ti-augite mantling and rims of clinopyroxene were crystallized in a low-pressure upper crust environment, the PN massif, whereas diopside antecrysts were formed in a hidden chamber at higher pressure, ~5.8 kbar, in the middle of the regional crust.

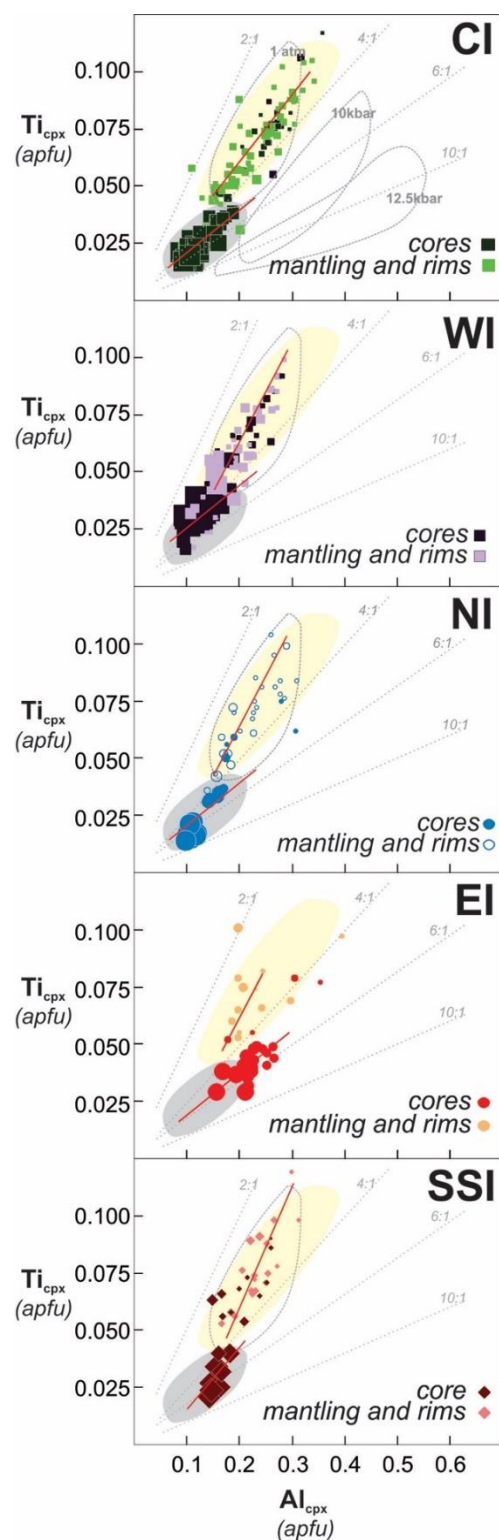


**Figure 10.** Ti versus Al (calculated to 6 oxygens) for the clinopyroxenes from the main intrusions of the PN massif, compared with the experimental data from [75] that correlates the proportion  $\text{Al}/\text{Ti}_{\text{cpx}}$  with pressure. The size of the symbols is related to the  $\text{Mg}_{\text{cpx}}$  content (higher  $\text{Mg}_{\text{cpx}}$ , bigger symbols). In this sense, high-Mg relict cores tend to present higher  $\text{Al}/\text{Ti}$  values than mantling and rims. Ti-augite mantling and rims in all intrusions are more compatible with low-pressure crystallization conditions, with diopside relict cores suggesting a deeper crystallization.

### 5.3. The Evolution of Hidden Chamber from PN

The petrological model of the PN massif [41] is assigned as repeated influxes of antecryst-laden basanite magmas. The primary cumulate intrusions of the massif deposit most of their suspended crystals on the floor of the upper-crust magma chamber. Each intrusion is representative of relatively primitive olivine- and clinopyroxene-phyric basanites that had assimilated different degrees of partial melts of heterogeneous host rocks [41,48]. The antecrysts presented in this work indicate that these influxes of antecryst-laden magmas could be derived from just one deeper magmatic chamber.

Clinopyroxenes of this hidden chamber have progressive enrichments of incompatible elements with the decrease in  $Mg\#_{cpx}$  (Figure 11), indicating that this deeper chamber was mainly controlled by typical fractional crystallization processes. The inflection points for Sr and REE are related to abrupt decreases in these elements, followed by progressive increases (Figure 11). These inflections could be due to the starting of co-precipitation of some mineral phases that have high mineral-melt partition coefficients for Sr and REE, such as plagioclase or apatite (e.g., [85–89]). In fact, part of the plagioclase and apatite crystals of PN are also attributed to minor components of the cumulus assemblage and also classified as antecrysts based on their in situ isotopic compositions [41]. In our study, few analyses of apatite and plagioclase (high-An) were presented (Supplementary Material G) as a reference for the incorporation of Sr and REE by these phases (Figure 12). Once plagioclase holds similar REE values to that of the high-Mg diopsides, it seems that these elements are mostly controlled by apatite (Figure 12). Otherwise, Sr contents are higher in apatite and plagioclase in relation to clinopyroxene antecrysts, and, therefore, simultaneous crystallization of these phases could be affected by the Sr concentration in clinopyroxenes. The evolution trend of antecrystic clinopyroxene indicates that the main intrusions of the shallow chamber, the PN massif, were fed by a single deeper hidden chamber mainly controlled by fractional crystallization processes.

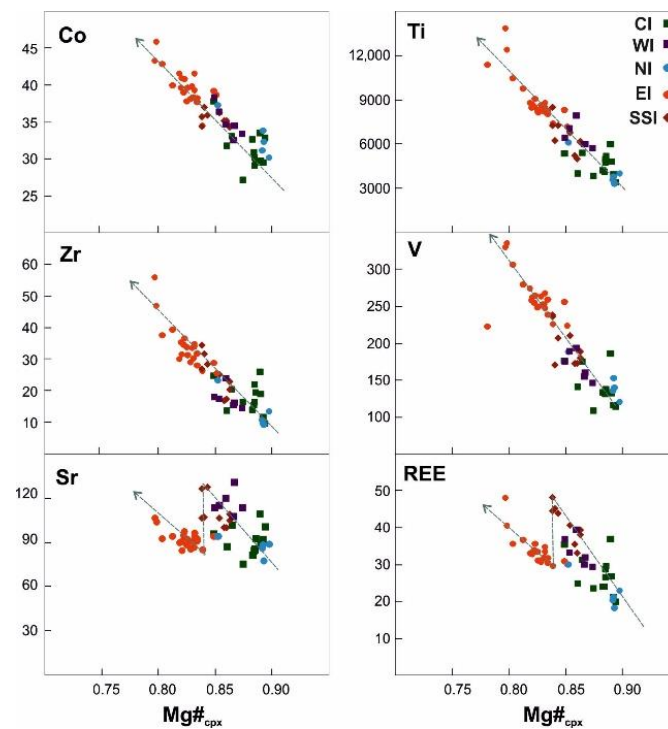


**Figure 11.** Diagrams of  $Mg\#_{cpx}$  vs. trace element compositions (ppm) for PN clinopyroxene relict cores (antecrysts). Incompatible trace elements present a clear negative correlation with  $Mg\#_{cpx}$  compositions, suggesting an evolution trend compatible with that expected for fractional crystallization

processes. In the case of PN, this antecryst evolution trend points to a deeper chamber evolution, before the formation of upper crust chamber. An inflection point is found for Sr and REE values with intermediate Mg#. This decrease and subsequent increase in Sr and REE values can be attributed to a subtle change in the trace elements concentrations in the evolving liquid, possibly due to the supersaturation of a new mineral phase in the liquid that incorporates these two elements.

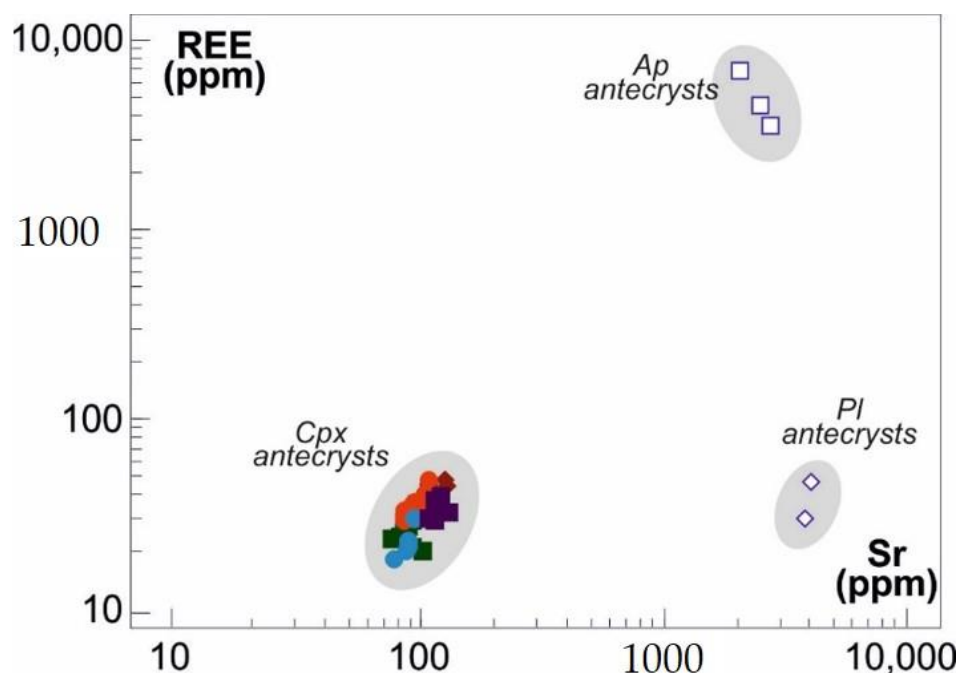


**Figure 12.** Diagrams of Sr (ppm) vs. REE (ppm) for PN clinopyroxene relict cores (antecrysts) compared with cumulated plagioclase and apatite compositions in PN. Symbols of clinopyroxenes as in Figure 11.

In each intrusion of PN, clinopyroxenes antecrysts representative of different degrees of magmatic differentiation of this deeper environment are found. Basic–ultrabasic dikes from the Mantiqueira Range present similar clinopyroxene and olivine antecryst population (Figure 8; [37]). Possibly, PN antecrysts are related to a similar plumbing system, although without its predicted interaction with evolved alkaline systems, as PN do not present the green core pyroxenes found in some occurrences of Mantiqueira region [37]. The evolution trend found for the diopside antecrysts (Figure 11) suggests that all the main intrusions of PN were possibly related to a single deeper hidden chamber that fed the intrusions of PN with crystals of different degrees of evolution (Figure 13).

On the other hand, the very similar compositional trends found for mantling and rims of clinopyroxene crystals from the different intrusions indicate similar liquid compositions that have crystallized in the shallow environment (Figures 4 and 11). In the upper crust chamber of the PN massif, corrosion and/or resorption/re-equilibration of antecrysts are common features; in fact, other differentiation processes (apart from crystal fractionation) have also acted in this upper-crust chamber, such as crustal assimilation [41,48]. Thus, the particular behavior of some elements in mantling and rims of clinopyroxenes of the EI, SSI and WI could be attributed to assimilation processes of the regional heterogeneous host rock, as evidenced by isotopic data [41]. As a result, many disequilibrium textures were found especially for the clinopyroxene. In the lower levels of each intrusion, however, better conditions for the preservation of such relict cores were found and the evidence of a hidden chamber has been presented.

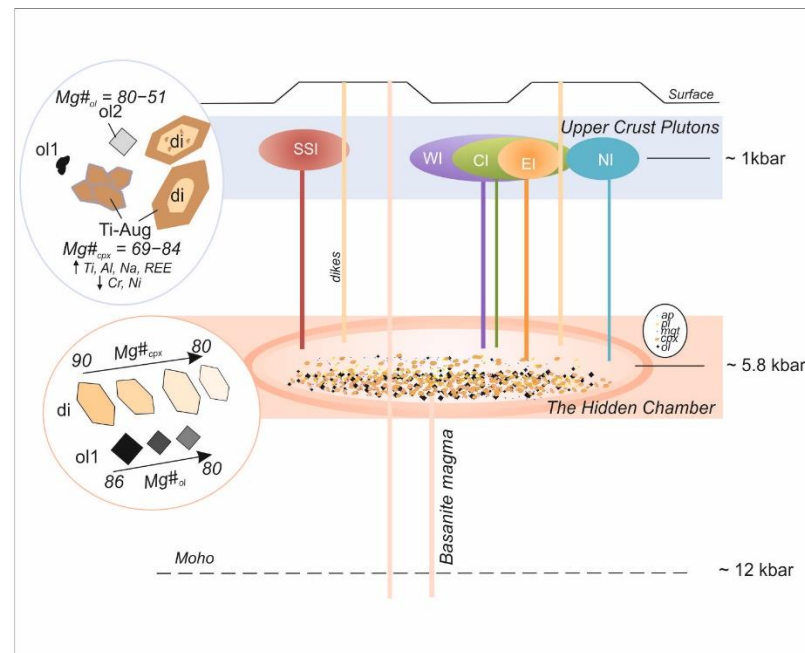


**Figure 13.** Schematic illustrating the proposed petrological model for the Ponte Nova mafic-ultramafic alkaline massif, outlined as repeated influxes of antecryst-laden basanite magma pulses. The antecryst assemblage is mainly formed by clinopyroxene (cpx), with subordinate olivine (Ol) and minor plagioclase (pl), apatite (ap) and Ti-magnetite (mgt). These minerals are the main cumulus phases found in the lower levels of the main cumulate intrusions of the massif and indicate a deeper hidden chamber for Ponte Nova massif. The ~5.8 kbar P estimation offered are relative to the calculations based on clinopyroxene-melt thermobarometry [66,68]. The dikes shown correspond to basic-ultrabasic dikes from the Mantiqueira Range, presenting similar clinopyroxene and olivine antecryst population. In the upper crust plutons of the Ponte Nova massif, corrosion and/or resorption/re-equilibration of antecrysts are a common feature, with mantled (growth type) by Ti-augite.

Finally, the PN massif represents a good example of transcrustal scale magmatic processes (i.e., plumbing systems; [6,90]), which lead to the formation of complex alkaline systems, and could improve the understanding of the evolution of mush-type reservoirs in typical anorogenic settings.

## 6. Conclusions

Clinopyroxene and olivine antecrysts are described for the first time in the plutons of the Ponte Nova alkaline mafic-ultramafic massif (SE Brazil). Diopside antecrystic cores (mostly partially corroded) present higher Mg, Cr, Ni and lower Ti, Na, Al, REE and Sr than Ti-augite mantling and rims. Subordinately, highly zoned olivine antecrysts have high Mg (Fo up to 86 mol.%) and Ni cores (mostly with corroded rims). Temperature and pressure estimates based on clinopyroxene-liquid geothermobarometers indicate crystallization of the antecrysts at  $\sim 1171 \pm 10$  °C and  $\sim 5.7 \pm 0.3$  kbar, pointing to a deeper hidden magmatic chamber, whereas mantling and rim compositions indicate a shallow chamber environment. Clinopyroxenes of this hidden chamber have progressive enrichments of incompatible elements with the decrease in Mg#, but with inflection points for Sr and REE mainly due to the starting of co-precipitation of apatite. The evolution trend of antecrystic clinopyroxene indicates that the main intrusions of the shallow chamber, the Ponte Nova massif, were fed by a single deeper hidden chamber mainly controlled by typical fractional crystallization processes. These antecrysts suggest the presence of a complex plumbing system, which is also supported by the similar antecrysts found in the lamprophyre and alkali basalt dikes of this region. The preferred petrological model for the Ponte Nova massif could be

summarized as repeated influxes of antecryst-laden basanite magmas that deposited most of their suspended crystals mainly on the floor of the upper-crust magma chamber.

**Supplementary Materials:** The following supporting information can be downloaded at: <https://www.mdpi.com/article/10.3390/min12060775/s1>, **A**—Tables of major element of clinopyroxene and olivine compositions from the Ponte Nova massif (MS-Excel file). Table SA1. Analytical parameters and calibration standards used for WDS analyses of clinopyroxene and olivine. Table SA2. Major element compositions in mass % of clinopyroxene from the Ponte Nova massif. Structural formula calculated on the basis of 6 oxygens. Abbrev.: c, cores; m/r, mantling/rims. Table SA3. Major element concentrations in mass % of olivine from the Ponte Nova massif. Structural formula calculated on the basis of 4 oxygens. Abbrev.: c, cores; r, rims. **B**—Compilation of whole-rock geochemical analyses from the Ponte Nova alkaline mafic–ultramafic massif. All data is compiled from Azzone et al., (2016; 2020). Samples in blue are those selected for trace element (LA-ICP-MS) mineral analyses, that presented important amounts of clinopyroxene and olivine antecrysts. For details of analytical methods and sample descriptions, please see the original source (Azzone et al., 2016; 2020). **C**—Clinopyroxene trace-element compositions from Ponte Nova Massif (MS-Excel file). Table SC1. Trace element compositions for BHVO-2G (USGS) calibration (primary) standard used for routines of trace element analyses of PN clinopyroxenes. Recommended values are from GeoReM, preferred values: 1/2009, Jochum (Max-Planck—Institut fuer Chemie); see Jochum et al., 2005. Table SC2. Trace element compositions for NIST SRM 612, BIR-1 and BCR-2 quality-control monitors (reference materials) used for routines of trace-element analyses of PN clinopyroxenes. Recommended values are from Jochum et al. (2015). Table SC3. Trace-element compositions for clinopyroxene crystals from PN massif. **D**—Olivine trace element compositions from Ponte Nova Massif (MS-Excel file). Table SD1. Trace element compositions for BCR-2G (USGS) calibration (primary) standard used for routines of trace element analyses of PN clinopyroxenes. Recommended values are from Jochum et al. (2011). Table SD2. Trace element compositions for BIR-1 quality-control monitor (reference material) used for routines of trace element analyses of PN olivines. Recommended values are from Jochum et al. (2015). Table SD3. Trace element compositions for olivine crystals from PN massif. **E**—Compositional variation of clinopyroxene crystals from the main intrusions of PN (MS-Word file).  $Mg\#_{cpx}$  vs trace element compositions (ppm) are presented, contrasting antecrystic relict cores (pale brown field) with Ti-augite mantling and rims. Mantling and rims indicate a progressive enrichment in incompatible elements (e.g., REE, Zr, Sr) and impoverishment in compatible ones (e.g., Ni) with the decrease in  $Mg\#_{cpx}$ . **F**—Calculated P and T parameters for the Ponte Nova antecrystic clinopyroxene/primitive liquids of Mantiqueira range pairs (MS-Excel file). Table SF1. CpxPN-Liq; Spreadsheet adapted from Neave et al. (2019), with the composition of 28 pairs of clinopyroxene relict cores of PN with putative liquid compositions (Mantiqueira range primitive dikes) used to estimate the crystallization pressure and temperature of the clinopyroxene antecrysts of PN. Table SF2. CpxDike-Liq; Spreadsheet adapted from Neave et al. (2019), with the composition of one pair of clinopyroxene-liquid from the Mantiqueira Range used to estimate the crystallization pressure and temperature of the dikes. Table SF3. Rhodes Diag Calc: The Rhodes diagram showing the  $K_D$  equilibrium test. Table SF4. DiHd, EnFs and CaTs Equilib: Multicomponent equilibrium diagram comparing predicted (theoretical calculated) clinopyroxene components with observed clinopyroxene components for DiHd, EnFs, and CaTs. **G**—Trace-element composition of plagioclase and apatite from Ponte Nova Massif (MS-Excel file). Procedures. Table SG1. Trace-element composition of NIST SRM 612 for calibration (primary) standard used in routines of trace-element analyses of plagioclase crystals from PN. Recommended values are from Jochum et al. (2011). Table SG2. Analyses of NIST SRM 610 for calibration (primary) standard used in routines of trace-element analyses of PN apatite. Recommended values are from Jochum et al. (2011). Table SG3. Analysis results of BHVO-2G for quality control of routine of trace-element analyses in plagioclase and apatite from PN. Recommended values are from GeoReM, preferred values: 1/2009, Jochum (Max-Planck—Institut fuer Chemie). Table SG4. Chemical composition of plagioclase crystals from PN. Table SG5. Chemical composition of apatite crystals from PN.

**Author Contributions:** Conceptualization, R.G.A.; investigation, R.G.A., M.R.A. and L.M.C.T.; data curation, all authors; writing—original draft preparation, all authors; writing—review and editing, all authors; visualization, R.G.A., L.M.C.T. and V.G.; project administration, R.G.A.; funding acquisition, R.G.A. and E.R. All authors have read and agreed to the published version of the manuscript.

**Funding:** São Paulo Research Foundation, FAPESP (Processes 2010/20425-8, 2017/03768-8, 2019/22084-8); Brazilian National Research Council—CNPq (Grant 310055/2021-0).

**Institutional Review Board Statement:** Not applicable.

**Informed Consent Statement:** Not applicable.

**Data Availability Statement:** Not applicable.

**Acknowledgments:** This research is funded by FAPESP (Procs. 2010/20425-8, 2017/03768-8, 2019/22084-8). RGA acknowledges the Brazilian National Research Council—CNPq for a productivity grant (310055/2021-0). CAPES is acknowledged for the doctoral scholarship for LMCT and MRA. We thank the analytical support of the technicians of the laboratories of GeoAnalítica-USP facilities and the contribution of some undergraduate students of our research group that followed and/or helped in part of the data acquisition steps. The authors appreciated and acknowledge the helpful comments and suggestions of the reviewers, and the editorial support from the journal.

**Conflicts of Interest:** The authors declare no conflict of interest.

## References

1. Sakuyama, M. Magma mixing and magma plumbing systems in island arcs. *Bull. Volcanol.* **1984**, *47*, 685–703. [[CrossRef](#)]
2. Marsh, B.D. Dynamics of magmatic systems. *Elements* **2006**, *2*, 287–292. [[CrossRef](#)]
3. Jerram, D.A.; Martin, V.M. Understanding crystal populations and their significance through the magma plumbing system. In *Dynamics of Crustal Magma Transfer, Storage and Differentiation*; Annen, C., Zellmer, G.F., Eds.; Geological Society of London: London, UK, 2008; pp. 133–148.
4. Ubide, T.; Arranz, E.; Lago, M.; Galé, C.; Larrea, P. The influence of crystal settling on the compositional zoning of a thin lamprophyre sill: A multi-method approach. *Lithos* **2012**, *132–133*, 37–49. [[CrossRef](#)]
5. Ubide, T.; Galé, C.; Larrea, P.; Arranz, E.; Lago, M. Antecrysts and their effect on rock compositions: The Cretaceous lamprophyre suite in the Catalonian Coastal Ranges (NE Spain). *Lithos* **2014**, *206–207*, 214–233. [[CrossRef](#)]
6. Cashman, K.V.; Sparks, R.S.J.; Blundy, J.D. Vertically extensive and unstable magmatic systems: A unified view of igneous processes. *Science* **2017**, *355*, eaag3055. [[CrossRef](#)]
7. Burchardt, S. *Volcanic and Igneous Plumbing Systems: Understanding Magma Transport, Storage, and Evolution in the Earth's Crust*; Elsevier: Uppsala, Sweden, 2018.
8. Jerram, D.A.; Bryan, S.E. Plumbing systems of shallow level intrusive complexes. In *Physical Geology of Shallow Magmatic Systems*; Breiterkreuz, C., Rocchi, S., Eds.; Springer: Cham, Switzerland, 2018; pp. 39–60.
9. Streck, M.J. Mineral textures and zoning as evidence for open system processes. *Rev. Mineral. Geochem.* **2008**, *69*, 595–622. [[CrossRef](#)]
10. Davidson, J.P.; Morgan, D.J.; Charlier, B.L. Isotopic microsampling of magmatic rocks. *Elements* **2008**, *3*, 253–259. [[CrossRef](#)]
11. Ubide, T.; McKenna, C.A.; Chew, D.M.; Kamber, B.S. High-resolution LA-ICP-MS trace element mapping of igneous minerals: In search of magma histories. *Chem. Geol.* **2015**, *409*, 157–168. [[CrossRef](#)]
12. Vernon, R.H.; Etheridge, M.A.; Wall, V.J. Shape and microstructure of microgranitoid enclaves; indicators of magma mingling and flow. *Lithos* **1988**, *22*, 1–11. [[CrossRef](#)]
13. Barbarin, B.; Didier, J. Genesis and evolution of mafic microgranular enclaves through various types of interaction between coexisting felsic and mafic magmas. *Trans. R. Soc. Edinb.* **1992**, *83*, 145–153.
14. Clarke, D.B. Assimilation of xenocrysts in granitic magmas: Principles, processes, proxies, and problems. *Can. Mineral.* **2007**, *45*, 5–30. [[CrossRef](#)]
15. Brandriss, M.E.; Mason, S.; Winsor, K. Rhythmic layering formed by deposition of plagioclase phenocrysts from influxes of porphyritic magma in the Cuillin Centre, Isle of Skye. *J. Petrol.* **2014**, *55*, 1479–1510. [[CrossRef](#)]
16. Wiebe, R.A. Mafic replenishments into floored silicic magma chambers. *Am. Mineral.* **2016**, *101*, 297–310. [[CrossRef](#)]
17. Franciosi, L.; D'Antonio, M.; Fedele, L.; Guarino, V.; Tassinari, C.C.G.; de Gennaro, R.; Cucciniello, C. Petrogenesis of the Solanas gabbro-granodiorite intrusion, Sàrrabus (southeastern Sardinia, Italy): Implications for Late Variscan magmatism. *Int. J. Earth Sci.* **2019**, *108*, 989–1012. [[CrossRef](#)]
18. Hibbard, M.J. Textural anatomy of twelve magma-mixed granitoid systems. In *Enclaves and Granite Petrology*; Didier, J., Barbarin, B., Eds.; Elsevier: Amsterdam, The Netherlands, 1991; pp. 431–444.
19. Hibbard, M.J. *Petrography to Petrogenesis*; Prentice Hall: Hoboken, NJ, USA, 1995.

20. Vernon, R.H. Crystallization and hybridism in microgranular enclave magmas: Microstructural evidence. *J. Geophys. Res.* **1990**, *95*, 17849–17859. [[CrossRef](#)]
21. Sarkar, C.; Storey, C.D.; Hawkesworth, C.J. Using perovskite to determine the pre-shallow level contamination magma characteristics of kimberlite. *Chem. Geol.* **2014**, *363*, 76–90. [[CrossRef](#)]
22. Dobosi, G.; Fodor, R.V. Magma fractionation, replenishment, and mixing as inferred from green-core clinopyroxenes in Pliocene basanite, southern Slovakia. *Lithos* **1992**, *28*, 133–150. [[CrossRef](#)]
23. Rock, N.M.S.; Gwalani, L.G.; Griffin, B.J. Alkaline rocks and carbonatites of Amba Dongar and adjacent areas, Deccan Alkaline Province, Gujarat, India. 2. Complexly zoned clinopyroxene phenocrysts. *Mineral. Petrol.* **1994**, *51*, 113–135. [[CrossRef](#)]
24. Simonetti, A.; Shore, M.; Bell, K. Diopside phenocrysts from nephelinite lavas, Napak Volcano, eastern Uganda; evidence for magma mixing. *Can. Mineral.* **1996**, *34*, 411–421.
25. Valente, S.C. Geochemical and Isotopic Constraints on the Petrogenesis of the Cretaceous Dykes of Rio de Janeiro, Brazil. Ph.D. Thesis, The Queen's University of Belfast, Belfast, Ireland, 1997.
26. Kahl, M.; Chakraborty, S.; Costa, F.; Pompilio, M. Dynamic plumbing system beneath volcanoes revealed by kinetic modeling, and the connection to monitoring data: An example from Mt. Etna. *Earth Planet. Sci. Lett.* **2011**, *308*, 11–22. [[CrossRef](#)]
27. Janckovics, M.É.; Taracsák, Z.; Dobosi, G.; Embey-Isztin, A.; Batki, A.; Harangi, S.; Hauzenberger, C.A. Clinopyroxene with diverse origins in alkaline basalts from the western Pannonian Basin: Implications from trace element characteristics. *Lithos* **2016**, *262*, 120–134. [[CrossRef](#)]
28. Gernon, T.M.; Upton, B.G.J.; Ugra, R.; Yücel, C.; Taylor, R.N.; Elliott, H. Complex subvolcanic magma plumbing system of an alkali basaltic maar-diatreme volcano (Elie Ness, Fife, Scotland). *Lithos* **2016**, *264*, 70–85. [[CrossRef](#)]
29. Ubide, T.; Gale, C.; Arranz, E.; Lago, M.; Larrea, P. Clinopyroxene and amphibole crystal populations in a lamprophyre sill from the Catalanian Coastal Ranges (NE Spain): A record of magma history and a window to mineral-melt partitioning. *Lithos* **2014**, *184*, 225–242. [[CrossRef](#)]
30. Batki, A.; Pál-Molnár, E.; Jankovics, M.É.; Kerr, A.C.; Kiss, B.; Markl, G.; Heincz, A.; Harangi, S. Insights into the evolution of an alkaline magmatic system: An in situ trace element study of clinopyroxenes from the Ditrău Alkaline Massif, Romania. *Lithos* **2018**, *300*, 51–71. [[CrossRef](#)]
31. Nakagawa, M.; Wada, K.; Wood, C.P. Mixed magmas, mush chambers and eruption triggers: Evidence from zoned clinopyroxene phenocrysts in andesitic scoria from the 1995 eruptions of Ruapehu volcano, New Zealand. *J. Petrol.* **2002**, *43*, 2279–2303. [[CrossRef](#)]
32. Tepley, F.J.; Davidson, J.P. Mineral-scale Sr-isotope constraints on magma evolution and chamber dynamics in the Rum layered intrusion, Scotland. *Contrib. Mineral. Petrol.* **2003**, *145*, 628–641. [[CrossRef](#)]
33. Miller, J.S.; Matzel, J.E.; Miller, C.F.; Burgess, S.D.; Miller, R.B. Zircon growth and recycling during the assembly of large, composite arc plutons. *J. Volcanol. Geotherm. Res.* **2007**, *167*, 282–299. [[CrossRef](#)]
34. Alves, A.; Janasi, V.A.; Pereira, G.S.; Prado, F.A.; Munoz, P.R.M. Unravelling the hidden evidences of magma mixing processes via combination of in situ Sr isotopes and trace elements analyses on plagioclase crystals. *Lithos* **2021**, *404–405*, 106435. [[CrossRef](#)]
35. Yuan, Q.; Namur, O.; Fischer, L.A.; Roberts, R.J.; Lü, X.; Charlier, B. Pulses of plagioclase-laden magmas and stratigraphic evolution in the Upper Zone of the Bushveld Complex, South Africa. *J. Petrol.* **2017**, *58*, 1619–1644. [[CrossRef](#)]
36. Cawthorn, R.G. Identification of Anorthite-enriched Plagioclase Antecrysts in the Bushveld Complex, South Africa. *J. Petrol.* **2019**, *60*, 1109–1118. [[CrossRef](#)]
37. Lopes, J.; Azzone, R.G.; Chmyz, L.; Guarino, V.; Lima, N.M. Mafic macrocrysts of ultrabasic alkaline dikes from the Mantiqueira Range, SE, Brazil: Tracers of a complex plumbing system. *Brazil. J. Geol.* **2020**, *50*, e20200010.
38. Azzone, R.G.; Ruberti, E.; Lopes, J.C.S.; Gomes, C.B.; Enrich, G.E.R.; Hollanda, M.H.B.M.; Tassinari, C.C.G. Upper Cretaceous weakly to strongly silica-undersaturated alkaline dike series of the Mantiqueira Range, Serra do Mar alkaline province: Crustal assimilation processes and mantle source signatures. *Brazil. J. Geol.* **2018**, *48*, 373–390. [[CrossRef](#)]
39. Azzone, R.G.; Ruberti, E.; Enrich, G.E.R.; Gomes, C.B. Geologia e geocronologia do maciço alcalino máfico-ultramáfico Ponte Nova (SP-MG). *Geol. USP Sér. Cient.* **2009**, *9*, 23–46. [[CrossRef](#)]
40. Gomes, C.B.; Comin-Chiaramonti, P. An introduction to the alkaline and alkaline-carbonatitic magmatism in and around the Paraná-Basin. In *Mesozoic to Cenozoic Alkaline Magmatism in the Brazilian Platform*; Comin-Chiaramonti, P., Gomes, C.B., Eds.; Edusp/Fapesp: São Paulo, Brazil, 2005; pp. 21–30.
41. Azzone, R.G.; Munoz, P.R.M.; Enrich, G.E.R.; Alves, A.; Ruberti, E.; Gomes, C.B. Petrographic, geochemical and isotopic evidence of crustal assimilation processes in the Ponte Nova alkaline mafic-ultramafic massif, SE Brazil. *Lithos* **2016**, *260*, 58–75. [[CrossRef](#)]
42. Morbidelli, L.; Gomes, C.B.; Beccaluva, L.; Brotzu, P.; Conte, A.M.; Ruberti, E.; Traversa, G. Mineralogical, petrological and geochemical aspects of alkaline and alkaline-carbonatite associations from Brazil. *Earth Sci. Rev.* **1995**, *39*, 135–168. [[CrossRef](#)]
43. Gomes, C.B.; Comin-Chiaramonti, P. *Magmatismo Alcalino Continental da Região Meridional da Plataforma Brasileira*; Edusp/Fapesp: São Paulo, Brazil, 2017.
44. Ulbrich, H.H.G.J.; Gomes, C.B. Alkaline rocks from continental Brazil. *Earth Sci. Rev.* **1981**, *17*, 135–154. [[CrossRef](#)]
45. Schobbenhaus, C.; Gonçalves, J.H.; Santos, J.O.S.; Abram, M.B.; Leão Neto, R.; Matos, G.M.M.; Vidotti, R.M.; Ramos, M.A.B.; Jesus, J.D.A. *Carta Geológica do Brasil ao Milionésimo—Folha SF-23*; Companhia de Pesquisa de Recursos Minerais, CPRM: Brasília, Brazil, 2004.

46. Almeida, F.F.M. Relações tectônicas das rochas alcalinas mesozóicas da região meridional da plataforma sul-americana. *Rev. Bras. Geociênc.* **1983**, *13*, 39–158. [[CrossRef](#)]
47. Vinagre, R.; Trouw, R.A.J.; Mendes, J.C.; Duffles, P.; Peternel, R.; Matos, G. New Evidence of a Magmatic Arc in the Southern Brasília Belt, Brazil: The Serra da Água Limpa Batholith (Socorro-Guaxupé Nappe). *J. S. Am. Earth Sci.* **2014**, *54*, 120–139. [[CrossRef](#)]
48. Azzone, R.G.; Chmyz, L.; Guarino, V.; Alves, A.; Gomes, C.B.; Ruberti, E. Isotopic clues tracking the open-system evolution of the Ponte Nova mafic-ultramafic alkaline massif, SE Brazil: The contribution of Pb isotopes. *Geochemistry* **2020**, *80*, 125648. [[CrossRef](#)]
49. Bastin, G.F.; Van Loo, F.J.J.; Heijligers, H.J.M. Evaluation and use of gaussian  $\Phi(\rho z)$  curves in quantitative electron probe microanalysis: A new optimization. *X-ray Spectrom.* **1984**, *13*, 91–97. [[CrossRef](#)]
50. Deer, W.A.; Howie, R.A.; Zussman, J. *An Introduction to the Rock-Forming Minerals*, 2nd ed.; Longman Scientific & Technical: London, UK, 1992.
51. Morimoto, N. Nomenclature of pyroxenes. *Mineral. Petrol.* **1988**, *39*, 55–76. [[CrossRef](#)]
52. Droop, G.T.R. A general equation for estimating  $\text{Fe}^{3+}$  concentrations in ferromagnesian silicates and oxides from microprobe analyses, using stoichiometric criteria. *Mineral. Mag.* **1987**, *51*, 431–435. [[CrossRef](#)]
53. Andrade, S.; Ulbrich, H.H.G.J.; Gomes, C.B.; Martins, L. Methodology for the determination of trace and minor elements in minerals and fused rock glasses with laser ablation associated with quadrupole inductively coupled plasma mass spectrometry (LA-Q-ICP-MS). *Am. J. Analyt. Chem.* **2014**, *5*, 701–721. [[CrossRef](#)]
54. Griffin, W.L. GLITTER: Data reduction software for laser ablation ICP-MS. In *Laser Ablation ICP-MS in the Earth Sciences*; Sylvester, P., Ed.; Short Course Series; Mineralogical Association of Canada: Ottawa, ON, Canada, 2008; pp. 308–311.
55. Xing, C.M.; Wang, C.Y. Periodic mixing of magmas recorded by oscillatory zoning of the clinopyroxene macrocrysts from an ultrapotassic lamprophyre dyke. *J. Petrol.* **2020**, *61*, ega103. [[CrossRef](#)]
56. Cao, G.; Xue, H.; Tong, Y. Complex magmatic processes recorded by clinopyroxene phenocrysts in a magmatic plumbing system: A case study of mafic volcanic rocks from the Laiyang Basin, southeastern North China Craton. *Lithos* **2022**, *416–417*, 106673. [[CrossRef](#)]
57. McDonough, W.F.; Sun, S. The composition of the Earth. *Chem. Geol.* **1995**, *120*, 223–253. [[CrossRef](#)]
58. Costa, F.; Dohmen, R.; Chakraborty, S. Time scales of magmatic processes from modeling the zoning patterns of crystals. *Rev. Mineral. Geochem.* **2008**, *69*, 545–594. [[CrossRef](#)]
59. Müller, T.; Dohmen, R.; Becker, H.W.; Ter Heege, J.H.; Chakraborty, S. Fe–Mg interdiffusion rates in clinopyroxene: Experimental data and implications for Fe–Mg exchange geothermometers. *Contrib. Mineral. Petrol.* **2013**, *166*, 1563–1576. [[CrossRef](#)]
60. Petrone, C.M.; Braschi, E.; Francalanci, L.; Casalini, M.; Tommasini, S. Rapid mixing and short storage timescale in the magma dynamics of a steady-state volcano. *Earth Planet. Sci. Lett.* **2018**, *492*, 206–221. [[CrossRef](#)]
61. Ganne, J.; Bachmann, O.; Feng, X. Deep into magma plumbing systems: Interrogating the crystal cargo of volcanic deposits. *Geology* **2018**, *46*, 415–418. [[CrossRef](#)]
62. Ubide, T.; Kamber, B.S. Volcanic crystals as time capsules of eruption history. *Nat Commun.* **2018**, *9*, 326. [[CrossRef](#)] [[PubMed](#)]
63. Brey, G.P.; Köhler, T. Geothermobarometry in four-phase lherzolites: II. New thermobarometers, and the practical assessment of existing thermobarometers. *J. Petrol.* **1990**, *31*, 1353e1378. [[CrossRef](#)]
64. Sharma, A.; Sahoo, S.; Rao, N.C.; Belyatsky, B.; Dhote, P.; Lehmann, B. Petrology and Nd–Sr isotopic composition of alkaline lamprophyres from the Early to Late Cretaceous Mundwara Alkaline Complex, NW India: Evidence of crystal fractionation, accumulation and corrosion in a complex magma chamber plumbing system. *Geol. Soc. Spec. Publ.* **2022**, *513*, 413–442. [[CrossRef](#)]
65. Rhodes, J.M.; Dungan, M.A.; Blanchard, D.P.; Long, P.E. Magma mixing at mid-ocean ridges: Evidence from basalts drilled near 228 N on the Mid-Atlantic Ridge. *Tectonophysics* **1979**, *55*, 35–61. [[CrossRef](#)]
66. Putirka, K.D. Thermometers and barometers for volcanic systems. *Rev. Mineral. Geochem.* **2008**, *69*, 61–120. [[CrossRef](#)]
67. Mollo, S.; Blundy, J.D.; Iezzi, G.; Scarlato, P.; Langone, A. The partitioning of trace elements between clinopyroxene and trachybasaltic melt during rapid cooling and crystal growth. *Contrib. Mineral. Petrol.* **2013**, *166*, 1633–1654. [[CrossRef](#)]
68. Neave, D.A.; Putirka, K.D. A new clinopyroxene-liquid barometer, and implications for magma storage pressures under Icelandic rift zones. *Am. Mineral.* **2017**, *102*, 777–794. [[CrossRef](#)]
69. Putirka, K.; Johnson, M.; Kinzler, R.; Longhi, J.; Walker, D. Thermobarometry of mafic igneous rocks based on clinopyroxene-liquid equilibria, 0–30 kbar. *Contrib. Mineral. Petrol.* **1996**, *123*, 92–108. [[CrossRef](#)]
70. Neave, D.A.; Bali, E.; Guðfinnsson, G.H.; Halldórsson, S.A.; Kahl, M.; Schmidt, A.S.; Holtz, F. Clinopyroxene-liquid equilibria and geothermobarometry in natural and experimental tholeiites: The 2014–2015 Holuhraun eruption, Iceland. *J. Petrol.* **2019**, *60*, 1653–1680. [[CrossRef](#)]
71. Putirka, K. Clinopyroxene+liquid equilibria to 100 kbar and 2450 K. *Contrib. Mineral. Petrol.* **1999**, *135*, 151–163. [[CrossRef](#)]
72. Yagi, K.; Onuma, K. The Join  $\text{CaMgSi}_2\text{O}_6$ – $\text{CaTiAl}_2\text{O}_6$  and its bearing on the Titanaugites. *J. Fac. Sci. Hokkaido Univ.* **1967**, *13*, 463–483.
73. Gibb, F.G. The zoned clinopyroxenes of the Shiant Isles sill, Scotland. *J. Petrol.* **1973**, *14*, 203–230. [[CrossRef](#)]
74. Wass, S.Y. Multiple origins of clinopyroxenes in alkali basaltic rocks. *Lithos* **1979**, *12*, 115–132. [[CrossRef](#)]
75. Thy, P. High and low pressure phase equilibria of a mildly alkalic lava from the 1965 Surtsey eruption: Experimental results. *Lithos* **1991**, *26*, 223–243. [[CrossRef](#)]

76. Adam, J.; Green, T.H. The effects of pressure and temperature on the partitioning of Ti, Sr and REE between amphibole, clinopyroxene and basanitic melts. *Chem. Geol.* **1994**, *117*, 219–233. [[CrossRef](#)]
77. Nimis, P. Clinopyroxene geobarometry of magmatic rocks. Part 2. Structural geobarometers for basic to acid, tholeiitic and mildly alkaline magmatic systems. *Contrib. Mineral. Petrol.* **1999**, *135*, 62–74. [[CrossRef](#)]
78. Brotzu, P.; Melluso, L.; Bennio, L.; Gomes, C.B.; Lustrino, M.; Morbidelli, L.; Morra, V.; Ruberti, E.; Tassinari, C.C.G.; D'Antonio, M. Petrogenesis of the Early Cenozoic potassic alkaline complex of Morro de São João, southeastern Brazil. *J. S. Am. Earth Sci.* **2007**, *24*, 93–115. [[CrossRef](#)]
79. Guarino, V.; Azzone, R.G.; Brotzu, P.; Gomes, C.B.; Melluso, L.; Morbidelli, L.; Ruberti, E.; Tassinari, C.C.G.; Brilli, M. Magmatism and fenitization in the Cretaceous potassium-alkaline-carbonatitic complex of Ipanema São Paulo State, Brazil. *Mineral. Petrol.* **2012**, *104*, 43–61. [[CrossRef](#)]
80. Guarino, V.; de' Gennaro, R.; Melluso, L.; Ruberti, E.; Azzone, R.G. The transition from miaskitic to agpaitic rocks as marked by the accessory mineral assemblages, in the Passa Quatro alkaline complex (southeastern Brazil). *Can. Mineral.* **2019**, *57*, 339–361. [[CrossRef](#)]
81. Guarino, V.; Lustrino, M.; Zanetti, A.; Tassinari, C.C.G.; Ruberti, E.; de' Gennaro, R.; Melluso, L. Mineralogy and geochemistry of a giant magma reservoir: The Late Cretaceous Poços de Caldas potassic alkaline complex (SE Brazil). *Lithos* **2021**, *398–399*, 106330. [[CrossRef](#)]
82. Hackspacher, P.C.; Ribeiro, L.F.B.; Ribeiro, M.C.S.; Fetter, A.H.; Hadler, J.C.; Tello, C.E.S.; Dantas, E.L. Consolidation and break-up of the South American platform in southeastern Brazil: Tectonothermal and denudation histories. *Gondwana Res.* **2004**, *7*, 91–101. [[CrossRef](#)]
83. Tello-Saenz, C.A.; Hackspacher, P.C.; Hadler, N.J.C.; Iunes, P.J.; Guedes, O.S.; Ribeiro, L.F.B.; Paulo, S.R. Recognition of Cretaceous, Paleocene, and Neogene tectonic reactivation through apatite fission-track analysis in Precambrian areas of southeast Brazil: Association with the opening of the south Atlantic Ocean. *J. S. Am. Earth Sci.* **2003**, *15*, 765–774. [[CrossRef](#)]
84. Hiruma, S.T.; Riccomini, C.; Modenesi-Gauttieri, M.C.; Hackspacher, P.C.; Hadler Neto, J.C.; Franco-Magalhães, A.O.B. Denudation history of the Bocaina Plateau, Serra do Mar, southeastern Brazil: Relationships to Gondwana breakup and passive margin development. *Gondwana Res.* **2010**, *18*, 674–687. [[CrossRef](#)]
85. Marks, M.; Halama, R.; Wenzel, T.; Markl, G. Trace element variations in clinopyroxene and amphibole from alkaline to peralkaline syenites and granites: Implications for mineral–melt trace-element partitioning. *Chem. Geol.* **2004**, *211*, 185–215. [[CrossRef](#)]
86. Prowatke, S.; Klemme, S. Trace element partitioning between apatite and silicate melts. *Geochim. Cosmochim. Acta* **2006**, *70*, 4513–4527. [[CrossRef](#)]
87. Mollo, S.; Forni, F.; Bachmann, O.; Blundy, J.D.; De Astis, G.; Scarlato, P. Trace element partitioning between clinopyroxene and trachy-phonolitic melts: A case study from the Campanian Ignimbrite (Campi Flegrei, Italy). *Lithos* **2016**, *252*, 160–172. [[CrossRef](#)]
88. Ladenburger, S.; Marks, M.A.; Upton, B.; Hill, P.; Wenzel, T.; Markl, G. Compositional variation of apatite from rift-related alkaline igneous rocks of the Gardar Province, South Greenland. *Am. Mineral.* **2016**, *101*, 612–626. [[CrossRef](#)]
89. Baudouin, C.; France, L.; Boulanger, M.; Dalou, C.; Devidal, J.L. Trace element partitioning between clinopyroxene and alkaline magmas: Parametrization and role of M1 site on HREE enrichment in clinopyroxenes. *Contrib. Mineral. Petrol.* **2020**, *175*, 42. [[CrossRef](#)]
90. Jackson, M.D.; Blundy, J.; Sparks, R.S.J. Chemical differentiation, cold storage and remobilization of magma in the Earth's crust. *Nature* **2018**, *564*, 405–409. [[CrossRef](#)]